

Deformation of nanocrystalline materials by molecular-dynamics simulation: relationship to experiments?

D. Wolf ^{a,*}, V. Yamakov ^b, S.R. Phillpot ^c, A. Mukherjee ^d, H. Gleiter ^e

^a Argonne National Laboratory, 9700 S. Cass Avenue, Argonne, IL 60439, USA

^b National Institute of Aerospace, Hampton, VA 23666, USA

^c Department of Materials Science and Engineering, University of Florida, Rhines Hall, Gainesville, FL 32611, USA

^d University of California, Davis, CA 95616, USA

^e Forschungszentrum Karlsruhe, Institut für Nanotechnologie, 76021 Karlsruhe, Germany

Received 7 May 2004; received in revised form 4 August 2004; accepted 23 August 2004

Available online 26 October 2004

Abstract

We review the results of recent molecular-dynamics simulations of the structure and deformation behavior of nanocrystalline materials, i.e., polycrystalline materials with a grain size of typically less than about 100 nm. These simulations have now become large enough and sophisticated enough that they are beginning to cover the entire range of grain sizes over which the experimentally suggested transition from a dislocation-based deformation mechanism to one involving GB processes takes place. Their atomic-level resolution provides novel insights into the intricate interplay between the dislocation and GB processes responsible for this crossover. These simulations also reveal how and why this crossover in the dominant mechanism leads to a transition in the mechanical behavior. However, in spite of these early successes, these simulations are inherently limited to rather idealized model microstructures and extremely high deformation rates. We therefore address the critical question as to the degree to which they begin to capture the experimentally observed, albeit controversial, deformation behavior of real nanocrystalline materials. (Supplementary material to this article, in the form of color graphs of some of the figures and several deformation-simulation movies, can be viewed at <http://phillpot.mse.ufl.edu/review.html>.)

© 2004 Acta Materialia Inc. Published by Elsevier Ltd. All rights reserved.

Contents

1. Introduction	2
2. Grain-boundary structural model for nanocrystalline materials by MD simulation.	5
2.1. Grain boundaries in coarse-grained materials.	5
2.1.1. Special high-angle boundaries	5
2.1.2. Dislocation boundaries.	5
2.1.3. General high-angle boundaries.	6
2.2. MD synthesis and characterization of nanocrystalline model microstructures	7
2.3. High-temperature grain-boundary structure and behavior	9
2.3.1. Grain-boundary migration and diffusion in bicrystals	10

* Corresponding author. Tel.: +1 630 252 5205; fax: +1 630 252 4798.

E-mail address: wolf@anl.gov (D. Wolf).

2.3.2.	Grain-boundary diffusion creep in nanocrystalline Pd	11
2.4.	Grain-boundary structural model for nanocrystalline materials	12
2.5.	Comparison with experiments.	12
2.6.	Critical issues and outstanding questions.	15
3.	Dislocation plasticity for larger grain sizes and existence of d_c	15
3.1.	Columnar simulation model for Al	15
3.2.	Length-scale effects in the nucleation of dislocations from the grain boundaries and existence of d_c	16
3.3.	Deformation twinning in nanocrystalline Al	17
3.4.	Comparison with experiments.	18
3.5.	Critical issues and outstanding questions.	20
4.	Grain-boundary based deformation mechanisms for the smallest grain sizes ($d < d_c$).	20
4.1.	Simulation of low-temperature deformation.	20
4.2.	Simulation of grain-boundary diffusion creep	22
4.3.	Geometrically necessary coupling between grain-boundary diffusion creep and grain-boundary sliding	23
4.4.	Discussion	23
4.5.	Comparison with experiments.	24
4.6.	Critical issues and outstanding questions.	26
5.	Crossover from ‘normal’ to ‘inverse’ Hall–Petch behavior.	27
5.1.	Grain boundaries as dislocation sources	27
5.2.	Crossover in the mechanical behavior	29
5.3.	Effect of the stacking-fault energy.	31
5.4.	Comparison with experiments.	33
5.4.1.	Normal and inverse Hall–Petch behavior.	33
5.4.2.	Microstructural observations.	35
5.5.	Critical issues and outstanding questions.	36
6.	Discussion and conclusions	36
	Acknowledgement	38
	References	38

1. Introduction

The structure and mechanical behavior of nanocrystalline materials have been the subject of considerable debate ever since polycrystalline metals with a grain size of typically less than 0.1 μm were first synthesized in bulk form approximately 20 years ago (for recent reviews see [1,2]). As far as the mechanical behavior is concerned, it is remarkable how little experimental information on the underlying GB and dislocation processes that control the deformation and fracture behavior of nanocrystalline materials has become widely accepted, the suggestions ranging from greatly enhanced ductility [3–5] to dramatically increased strength and hardness due to the Hall–Petch effect [6,7]. What seems to be more or less accepted, however, is that (a) for the larger grain sizes (of 50–100 nm) deformation is dominated by dislocation processes and (b) in the lower

grain-size range (<30 nm) a GB-based deformation process takes over, leading to a reduction of the yield and flow stress with decreasing grain size [8–15]; this phenomenon is known as the “inverse Hall–Petch effect”. The crossover from “normal” to “inverse” Hall–Petch behavior at a critical grain size, d_c , of typically 20–30 nm, observed in some experiments [13–15], is therefore thought to be due to a change in the dominant deformation mechanism, from one based on dislocations to one mediated by GB processes. The existence of such a crossover implies that a “strongest grain size” [6,16] exists at which the material is hardest to deform. This has driven the field forward, not only because of the potential exploitation of this effect in mechanical applications but also for fundamental scientific reasons.

Concerning the structure of these materials, the experimental situation is not much clearer [1,2]. Whereas the early studies [17,18] suggested a “frozen-

gas” like structure (lacking both short- and long-range order), more recent work has focused on the relationship between nanocrystalline microstructures and coarse-grained polycrystals, as well as their relation to amorphous solids. Two key questions that have thus emerged are (i) whether and under what conditions the atomic structure of the grain boundaries (GBs) in nanocrystalline materials can be extrapolated from those in coarse-grained polycrystals and bicrystals, and (ii) what the structural and thermodynamic relationship is between nanocrystalline microstructures and amorphous solids. However, in spite of a large body of experimental work, a GB structural model consistent with the many contradictory observations has not evolved. This is mostly because nanocrystalline microstructures are so extremely inhomogeneous and the type of local information needed to develop a detailed structural model is not easily obtainable by experimental means. Even in coarse-grained polycrystals, considerable difficulties exist in fully characterizing the microstructure as well as the atomic structure and chemistry of the interfaces; these problems are significantly enhanced by a submicron grain size.

Without a structural model for nanocrystalline materials, their mechanical behavior is difficult to rationalize. This is the reason why our overview begins with a description of the insights gained from recent computer simulations on the structure of nanocrystalline materials, with particular emphasis on the structure of the GBs and their relationship to amorphous structures and to the better-known structures of the GBs in coarse-grained polycrystals. With this perspective we will lay the foundation for the in-depth discussion of the mechanical behavior, which represents the main body of this paper.

Given the extremely rapid increases in recent years in processor speed coupled with the development of ever larger massively parallel computing architectures, atomic-level simulations have begun to provide novel insights into the structure and thermo-mechanical behavior of nanocrystalline materials. While the first simulations involved relatively modest system sizes [19–21], simulations have recently advanced to a level where they provide a powerful new tool for elucidating – in a degree of detail not possible experimentally – the atomic-level mechanisms controlling the complex dislocation and GB processes in heavily deformed materials with a submicron grain size. In particular, these simulations have now become large enough that they begin to capture the entire range of grain sizes where the transition from a dislocation to a GB-based deformation mechanism occurs.

Among the various atomic-level simulation approaches developed during past decades, including lattice statics, lattice dynamics, Monte Carlo and molecular dynamics (MD), the latter has proven partic-

ularly useful for the investigation of plastic deformation. Based on the solution of Newton’s equations for a system of atoms interacting via some prescribed interatomic interaction potential function, MD simulations are capable of exposing the real-time behavior during the deformation and include the effects of lattice anharmonicity, the highly inhomogeneous internal stresses, and the transient responses of the system as it probes and traverses complex, often unanticipated saddle-point configurations. (For an overview, see [22].)

Apart from their atomic-level spatial and temporal resolution, several unique features of MD simulations are particularly relevant to the deformation studies reviewed here. One is their ability to elucidate the behavior of a fully characterized, albeit usually idealized, nanocrystalline model system in terms of the underlying interfacial structure, driving forces and atomic-level mechanisms. Another arises from the ability to deform to rather large plastic strains, thus enabling the observation of deformation under very high GB and dislocation densities. This enables identification of the intra- and intergranular dislocation and GB processes in a deformation regime where they compete on an equal footing, thus providing atomic-level insights into the underlying mechanisms not available from experiments. Recent successes include, for example, identification of the atomic-level mechanisms for dislocation nucleation from, and annihilation at, the GBs [23–25]; the prediction [26] and recent experimental verification [27] of mechanical twinning in nanocrystalline Al [28]; elucidation of the mechanistic causes for the crossover from a dislocation to a GB-based deformation mechanism with decreasing grain size [29]; the observation of shear bands [30] and their relation to dimpled fracture surfaces [31].

In addition to being limited to relatively small model systems consisting of typically millions of atoms, the fundamental limitations inherent to the MD approach are well known, pertaining mainly to the reliability of the interatomic potentials used and the relatively short time period (of typically 10 ns, or about 10^7 MD time steps) over which the dynamics of the system can be probed. The interatomic force descriptions used in most MD simulations are of empirical or semi-empirical origin. While these have the advantage of being computationally extremely efficient, they are unable to fully capture the many-body nature of electronic bonding, particularly its complex, self-consistent variation as a function of local structure and chemistry in the vicinity of defects. Many-body potentials derived, for example, by means of the embedded-atom-method (EAM) by Daw and Baskes [32] incorporate at least to some degree the many-body nature of electronic bonding. Interestingly, however, extensive comparisons between many-body and pair potentials used in simulations of GBs in fcc and bcc metals [33] revealed few qualitative differences in the behavior predicted by these distinct force

descriptions, suggesting that many-body effects may not dominate GB behavior. (For a review of interatomic potentials used in atomistic simulations and a discussion of their limitations, see e.g. [34].)

The short time duration to which MD simulations are inherently limited is particularly relevant to the simulation of plastic deformation. As a consequence, such simulations always involve extremely high strain rates (of typically $>10^7/\text{s}$, corresponding to 1% strain in 1 ns), i.e., many orders of magnitude higher than in experiments. To render the deformation observable within such a short observation window, rather high stresses, usually much larger than in experiments, have to be applied. In order to avoid probing unphysical behavior, it is critical that in each simulation the applied stress is verified to lie well below the theoretical shear strength of the material in the particular direction of straining. It is also essential that the time scale(s) on which the simulated behavior occurs (e.g., the velocity of gliding dislocations) is verified to lie well below any critical inherent time scale(s) of the material (such as the speed of sound). We note, however, that high deformation stresses are not entirely unusual in experimental studies of nanocrystalline materials. For example, recent experiments on nanocrystalline Ni_3Al [35,36] show dislocation nucleation and propagation for a grain size of 50 nm at a stress of 1.5 GPa, i.e., very similar to typical MD stresses.

The issue of the high strain rates in MD simulations and the question as to whether they can actually capture experimentally observed deformation processes were addressed when MD simulations of nanocrystalline materials first became feasible [37]. As first proposed by Gleiter and his co-workers [3,8,9], the extrapolation of the Coble-creep formula [38] describing GB diffusion creep in coarse-grained materials to a nm grain size predicts extremely high strain rates, well within the MD range. To test whether MD simulations can, indeed, capture this well-known deformation process, Koblinski et al. [37] simulated GB diffusion creep in nanocrystalline-Si model microstructures that were tailored to (i) suppress grain growth (by selecting a uniform grain size and grain shape), and (ii) facilitate GB diffusion controlled deformation (by designing mostly high-energy GBs into the microstructure). Indeed, in spite of the extremely high strain rates (of $>10^8/\text{s}$), these simulations *quantitatively* validated the Coble-creep equation [38]. However, as recently discussed in some detail [39], special care must be taken, particularly in low-temperature simulations, to ensure that a GB or dislocation process that might dominate the deformation under experimental observation conditions is not inadvertently suppressed, and hence overlooked. The challenge is therefore to identify the real physical processes and avoid capturing a poorly defined, deformation-rate dependent transient response during the short MD time window.

In spite of these limitations inherent to the MD approach, the large-scale MD simulations of nanocrystalline microstructures reviewed in this article clearly represent a promising step towards elucidating the physics controlling the response of nanocrystalline microstructures to the driving forces of stress and temperature. However, given the highly idealized microstructures considered in such simulations, a key question concerns the degree to which they begin to capture the behavior of real materials. On the one hand, one wonders how incorporation of realistic distributions in the grain size and grain shape and of the effects of impurities inevitably present in real materials will affect the results. On the other hand, the experimental approaches against which the simulation results might be validated suffer from severe limitations as well, one of the greatest difficulties being associated with producing artifact-free samples. For example, processing methods starting with powders obtained by inert-gas condensation or mechanical attrition and subsequent compaction are susceptible to problems of porosity or incomplete particulate bonding [2,40]. Other processing routes also have drawbacks: there is a lower limit (of ~ 50 nm) to grain refinement in samples produced by severe plastic deformation; in crystallization of metallic glass, retention of amorphous structure remains a problem; magnetron sputtering yields a columnar (non-random) microstructure as does electrodeposition, which can also pick up the chemical signature of the electrolytic bath in the GBs. Furthermore, very often the experimental grain-size distribution is obtained by annealing; this annealing can produce changes in GB structure, result in stress relief and, in multiphase materials, produce changes in composition and morphology. Finally, the reported grain sizes are often measured either by analysis of XRD line broadening or TEM examination, and often there are large differences in the values measured by the two methods [41].

Given these limitations inherent to both the simulations and the experiments, few direct comparisons between simulations and experiments have been performed to date. Therefore, in addition to providing an overview of the present status of the MD simulations of the deformation behavior of nanocrystalline materials, another goal of this review is to offer a perspective on these simulation results in the context of pertinent experiments; for another recent perspective on the mechanical properties of nanocrystalline materials, see [42]. By assessing the experimental support for certain key predictions from the simulations, we hope to demonstrate that these simulations have now reached a level of fidelity where they begin to provide meaningful, novel atomic-level insights into dislocation and GB processes in nanocrystalline materials not readily obtainable from experiments, and with a degree of mechanistic detail unimaginable only a few years ago. Complementary to the experiments, these insights can therefore not only

provide valuable guidance towards sorting through the large, often contradictory body of experimental information but also expose the underlying concepts governing the complex interplay between dislocation and GB processes. We thus hope to offer a glimpse of how, in the near future, such simulations may revolutionize our understanding of plastic-deformation processes in heavily deformed materials. Following further experimental validation of key predictions from these simulations in the near future, it should soon be possible to elucidate the physical mechanisms controlling technologically important processes, such as superplastic forming. Moreover, the ability of such simulations to completely characterize the highly inhomogeneous state of internal stress will undoubtedly spur the development of better materials-physics based deformation models.

The paper is organized as follows. In Section 2, we review the simulations that have led to a first structural model for nanocrystalline materials, including their structural and thermodynamic relation to amorphous solids and to GBs in coarse-grained materials. In Section 3, we discuss the insights into dislocation plasticity gained from MD simulations of columnar microstructures with the largest grain sizes ($d > d_c$, for up to $d \sim 0.1 \mu\text{m}$). While the high degree of periodicity imposed in the columnar direction restricts the dislocations to being straight lines rather than loops, these simulations have the advantage of enabling rather large grain sizes to be considered and they are easily visualized and quantified. Although the lack of dislocation-line curvature in such columnar-model simulations fails to reproduce the grain-size dependence of the nucleation stress in the bulk material, we demonstrate the experimental support gained for some of the key predictions from these simulations. Section 4 focuses on the GB-based deformation processes in materials with the smallest grain sizes ($d < d_c$) and the insights gained from these simulations on the “inverse Hall–Petch effect”. In Section 5, we discuss recent simulations on fully 3d microstructures, which, for the first time, capture the full range of grain sizes where the crossover from a dislocation to a GB-based deformation process takes place with decreasing grain size.

2. Grain-boundary structural model for nanocrystalline materials by MD simulation

In spite of the large amount of experimental work on the structure and on structure-sensitive properties of nanocrystalline materials performed to date, a GB structural model consistent with the often contradictory observations has not evolved. However, without such a model it is difficult to rationalize experiments on structure-sensitive properties. Two key questions that have evolved from experimental studies are:

- (1) To what extent can the atomic structure of the GBs in nanocrystalline materials be extrapolated from those of coarse-grained polycrystalline materials and bicrystals?
- (2) What is the structural and thermodynamic relationship between nanocrystalline microstructures and amorphous solids?

In this section, we review the insights gained from atomic-level computer simulations on these two important questions and summarize the experimental situation.

2.1. Grain-boundaries in coarse-grained materials

A coarse-grained polycrystal contains GBs with very differing structures and a wide spectrum of energies and properties. In close analogy to the classification of the structure of free surfaces, much work of recent years has suggested the usefulness of distinguishing among the following three different types of GBs: Special high-angle GBs (analogous to flat surfaces), dislocation boundaries (analogous to stepped surfaces), and general high-angle GBs (analogous to surfaces with overlapping steps). (For a recent review, see [43].)

2.1.1. Special high-angle boundaries

Just as flat surfaces contain no steps, *special high-angle GBs* contain no dislocations. These boundaries give rise to energy cusps in the GB-misorientation phase space. The absence of dislocations in their atomic structure yields properties that are very much perfect-crystal like; i.e., their diffusivity and mobility are very low while their sliding resistance and cohesion are very high. In practice, in many respects a polycrystalline microstructure therefore evolves under the driving forces of temperature and stress as though these GBs are not present at all, with a correspondingly larger effective grain size. A notable exception in nanocrystalline fcc metals are the coherent and incoherent twin boundaries, which play an important role in the process of deformation twinning [44].

2.1.2. Dislocation boundaries

By analogy with stepped or vicinal surfaces, *dislocation boundaries* are “low-angle” or “vicinal” interfaces whose atomic structure consists of periodic arrays of dislocations that accommodate the deviation from the perfect crystal or from a “special”, i.e., cusped, GB misorientation [45]. For small vicinal deviations from a special GB-plane orientation or from a particularly small GB planar unit cell, dislocations separated by elastically strained perfect-crystal regions are formed to accommodate the misfit between the two grains. As in the case of vicinal surfaces [46], the energy and physical properties of dislocation boundaries can be expressed in terms of

the misorientation angle and axis characterizing the vicinal deviation from a nearby “special” interface, i.e., in terms of the structure and properties of isolated lattice dislocations and their elastic interaction [45].

2.1.3. General high-angle boundaries

The least well understood of the three types of GBs are the general high-angle GBs, i.e., GBs with completely overlapping dislocation cores. Although in practice, this type usually represents only a relatively small fraction of the GBs in a coarse-grained polycrystal, the pronounced properties of these GBs, particularly their high mobility and diffusivity coupled with a low sliding resistance and cohesion, can dominate the evolution of polycrystalline microstructures [47]. There has been much debate on their distinction from dislocation GBs, particularly on whether a dislocation picture is appropriate at high angles where the dislocation cores overlap completely. For example, in 1952 Smith [48] suggested that “...there is a continuous transition from the pure dislocation boundary to whatever exists at higher angles...”, and he suggested that the experimental evidence “...does not in any way preclude a nearly horizontal curve of energy vs. misorientation once the maximum value has been achieved”, implying that the energy of high-angle GBs is independent of the misorientation between the grains. That Smith’s intuition was correct was confirmed by extensive simulations of GB energies [33], revealing that there are, indeed, many high-angle GBs whose energy is entirely misorientation-independent.

Because the atomic structure of these GBs consists of completely overlapping dislocation cores, the GB structural disorder is distributed rather homogeneously, in a manner analogous to the surfaces of amorphous materials [49]. By contrast, similar to stepped surfaces, in dislocation boundaries the structural disorder is inhomogeneously distributed, consisting of well-defined, usually highly disordered dislocation cores separated by elastically distorted, perfect-crystal like regions [45].

To determine how the atomic structures of these “true” high-angle GBs depend on the GB energy, Keblinski et al. [50] considered high-angle twist GBs on the (1 1 1), (1 0 0) and (1 1 0) planes. It had been previously demonstrated that high-angle twist boundaries on these planes, the three densest in the fcc lattice, cover the entire spectrum of GB energies possible for fcc metals [33]. Whereas due to their large interplanar spacing parallel to the GB plane, GBs on the two densest planes of the fcc lattice, (1 1 1) and (1 0 0), have low and intermediate energies, respectively, GBs on the third densest, (1 1 0), plane already have very high energies and are, in fact, representative of the highest-energy GBs in fcc metals [33]. As representative high-angle twist GBs on these three planes, Keblinski et al. chose the (1 1 1) $\phi = 42.10^\circ$ ($\Sigma 31$), the (1 0 0) $\phi = 43.60^\circ$ ($\Sigma 29$) and the

(1 1 0) $\phi = 50.48^\circ$ ($\Sigma 11$) twist boundaries, where ϕ is the twist angle and Σ is the inverse density of coincident-site lattice (CSL) sites.

The degree of structural disorder at the GB is readily characterized in terms of local radial distribution functions, $g(r)$, for the lattice planes in the center of the GB. Fig. 1 shows the local structures of these GBs in Pd determined by a high-temperature equilibration MD method followed by slow cooling to zero temperature [50]. This is to be compared with the radial distribution function of bulk amorphous Pd determined by rapidly quenching the melt to 0 K, followed by relaxation of the forces on the atoms and the stress on the simulation cell [50].

As expected, the GB radial distribution functions for the low- and intermediate-energy GBs in Fig. 1(a) and

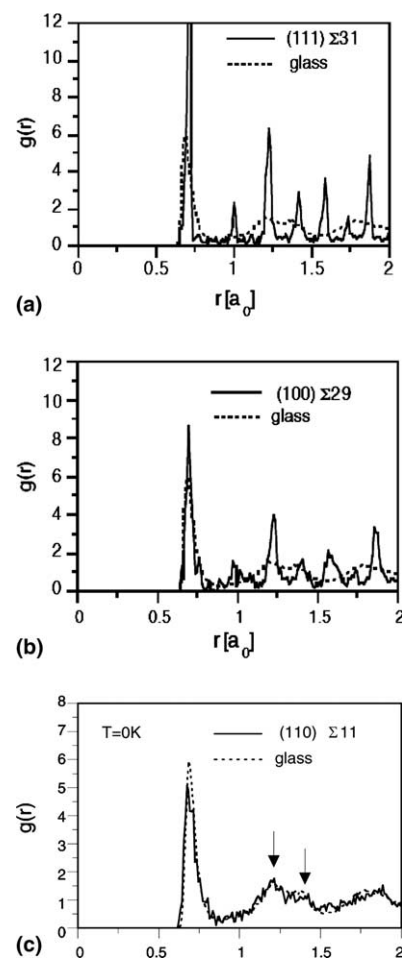


Fig. 1. Local radial distribution functions, $g(r)$, for high-angle twist GBs on the three densest lattice planes of fcc Pd, described by an EAM potential [55]. ($g(r)$ is normalized such that for large r , $g(r) = 1$.) For comparison, the dashed line shows $g(r)$ for the bulk Pd glass [50]. (a) (1 1 1) $\phi = 42.10^\circ$ ($\Sigma 31$) twist boundary with an energy of 300 mJ/m²; (b) (1 0 0) $\phi = 43.60^\circ$ ($\Sigma 29$) twist boundary with an energy of 800 mJ/m²; (c) (1 1 0) $\phi = 50.48^\circ$ ($\Sigma 11$) twist boundary with an energy of 1025 mJ/m². The arrows in (c) indicate the familiar split second peak present in both the GB and the bulk glass.

(b), (1 1 1) $\Sigma 31$ and (1 0 0) $\Sigma 29$ with energies of 300 and 800 mJ/m², respectively, reveal sharp peaks indicating the presence of long-range order in the GBs. By contrast, in the high-energy, (1 1 0) $\Sigma 11$ GB in Fig. 1(c) (with an energy of 1025 mJ/m²), $g(r)$ reveals a virtually complete absence of long-range order within the GB plane and is indistinguishable from that of the bulk Pd glass [50]. These results for fcc Pd are qualitatively identical to previous, more extensive simulations performed on GBs in Si [51,52].

2.2. MD synthesis and characterization of nanocrystalline model microstructures

In a first attempt to use atomistic simulations to develop a structural model for nanocrystalline materials, microstructures were synthesized by MD simulation of a supercooled melt into which small crystalline seeds with more or less random orientations had been inserted [19,20]. The subsequent crystal-growth simulation resulted in fully dense, impurity and porosity-free microstructures with fully equilibrated GBs that were subjected to full structural characterization.

Fig. 2 shows a cross-section through an fcc microstructure thus synthesized [19,20]. The two crystallites in the lower half of the figure are of particular interest as their seeds were oriented so as to form a coherent twin boundary (i.e., the symmetric tilt boundary on the (1 1 1) plane of the fcc lattice). In its optimum translational state, this GB has mirror-plane symmetry and, hence, an extremely low energy (of 1 mJ/m² for the Lennard-Jones potential used in these simulations). This en-

ergy is so low because only the third-nearest neighbors of the atoms at the GB are affected by the presence of the interface. However, in these simulations a small rigid-body translation away from the optimum, mirror-plane translational state was imposed on the original seeds; such translations might be present during the initial stages of the powder processing of nanocrystalline materials. The simulations revealed that this translation could not be optimized during the crystal-growth simulation, resulting in the highly disordered structure of this GB seen in Fig. 2, with the rather high energy of 701 mJ/m² for the same Lennard-Jones potential. This high energy arises from the highly constrained nanocrystalline microstructure, in which the rigid-body translations of the grains parallel to the GB plane cannot be fully optimized, by contrast with an entirely unconstrained GB in a bicrystal.

The GB disorder in this nanocrystalline microstructure was characterized in a rather simplistic way involving nearest-neighbor (nn) coordination, by simply determining the number of missing or extra nearest neighbors of each atom. In their first study of the deformation of nanocrystalline materials, Schiotz et al. [23] applied the much more powerful method of common-neighbor analysis (CNA) in which atoms are characterized as being either in a perfect-crystal fcc environment, in an hcp environment (distinguished from fcc by the third neighbors) or miscoordinated (see Fig. 3).

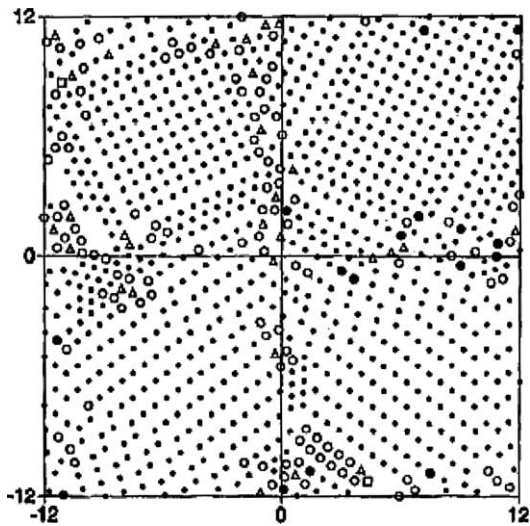


Fig. 2. Structural cross sections of thickness $0.4a_0$ through the centers of four of the eight grains in the cubic, 3d periodic simulation cell ($a_0 = 3.616$ Å is the lattice parameter of the LJ potential for Cu used in these simulations). The different symbols denote different nn miscoordinations, ranging between -3 (open squares), -2 (open triangles), -1 (open circles), 0 (small dots) and $+1$ (solid circles). (For more details, see [20].)

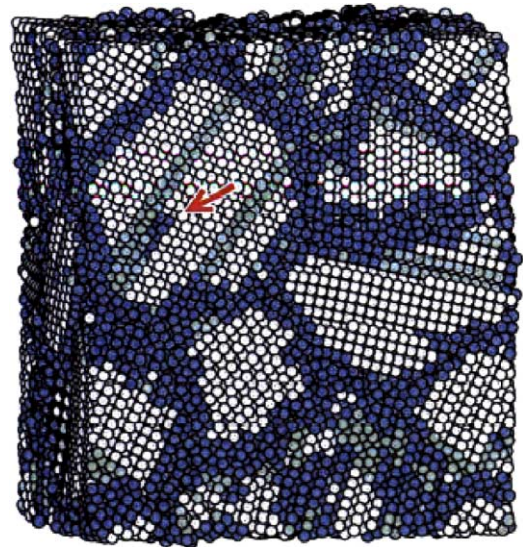


Fig. 3. Structural characterization of a deformed nanocrystalline microstructure using common neighbor analysis (CNA). The atoms with perfect fcc coordination are shown as white, those that are miscoordinated in the first neighbor shell are shown as dark blue. The atoms shown as light blue have perfect hcp coordination, which differs from fcc coordination only in the third neighbor shell. (For interpretation of the references to color in this figure legend, the reader is referred to the Web version of this article.)

The extension of the work on fcc metals to silicon [51–53] further elucidated the connection between the GBs present in nanocrystalline and coarse-grained microstructures. The simulations of nanocrystalline Si [53], involving grain sizes of up to about 7 nm, revealed the presence of highly disordered GBs with a more or less uniform thickness. For comparison, extensive simulations of microstructurally unconstrained, bicrystalline Si GBs [51,52] revealed a universal, highly disordered atomic structure of all the high-angle, *high-energy* GBs. Quantitative structural characterization in terms of $g(r)$ revealed that this universal structure was virtually indistinguishable from that of both the GBs present in nanocrystalline Si with random grain orientations and bulk amorphous Si (compare with Fig. 1(c) for Pd) [51,52]. By contrast, high-angle but *low-energy* bicrystalline GBs were found to exhibit good crystallinity (cf. Fig. 1(a) and (b)).

This work also revealed that the disordering of the high-energy GBs is driven by a lowering of the GB energy. It was therefore concluded that the existence of a highly disordered (confined amorphous) GB phase represents a thermodynamic rather than kinetic effect. This work also demonstrated that nanocrystalline-Si microstructures with randomly oriented grains contain mostly high-energy, large-unit-cell or incommensurate GBs with atomic structures that are qualitatively identical to those of *high-energy bicrystalline* GBs [19,20,51,52,54].

Similar simulations for nanocrystalline Pd [50] using the same Pd (EAM) potential [55] as in Fig. 1 yielded qualitatively identical results although, by contrast with Si, fcc metals do not have a stable bulk amorphous phase in terms of which the degree of GB structural disorder can be quantified. However, as described in Section 2.1, by rapidly quenching the melt a well-characterized bulk glass structure can be produced which is useful for analyzing GB structural disorder. As in the Si simulations [53], the three-dimensionally (3d) periodic, cubic simulation cell used in these simulations contained four randomly oriented seed grains in an fcc arrangement; these seeds were embedded in the melt filling the rest of the cell. The fully dense microstructure thus obtained after the crystal-growth simulation consists of dodecahedral grains delimited by GBs, triple lines and higher-fold point junctions [50]. In order to generate a driving force for crystal growth, the melt containing the seeds was cooled down to 800 K (i.e., well below the melting point of $T_m \sim 1500$ K [54,55]). The entire system (melt plus seeds) was subsequently allowed to evolve freely at constant temperature and under zero pressure. To ensure that the microstructure thus obtained was indeed stable, prior to structural characterization the sample was subjected to thermal annealing at 600 K under zero external stress for 30,000 MD steps, followed again by cooling to 0 K. The final structure

thus obtained, with a grain size of 8 nm, was found to be practically the same as the unannealed one, demonstrating that it is thermally stable against, for example, grain growth, at least on an MD time scale.

To characterize the microstructures thus obtained, planar cuts of thickness a_0 were made. Fig. 4(a) shows gray-scale contours of equal energy per atom for a slice parallel to the microstructural (1 1 1) planes; due to the 3d periodicity imposed on the simulation cell, this cut slices through all four grain centers. Clearly all GBs (seen as dark regions) have roughly the same width, while the triple lines appear to be slightly wider. Although the grain interiors appear to be perfect-crystal like, close inspection reveals a number of (1 1 1) twins developed during the growth process. Their formation is not surprising due to their extremely low energy (of ~ 3 mJ/m² for this Pd potential); this low energy is also the reason that they are not visible in the energy contour plot [50].

The average structure of the material as characterized by the system averaged, *overall* radial distribution function, $g(r)$, is shown in Fig. 5(a). The sharp crystalline peaks originate from the ordered grain interiors; the

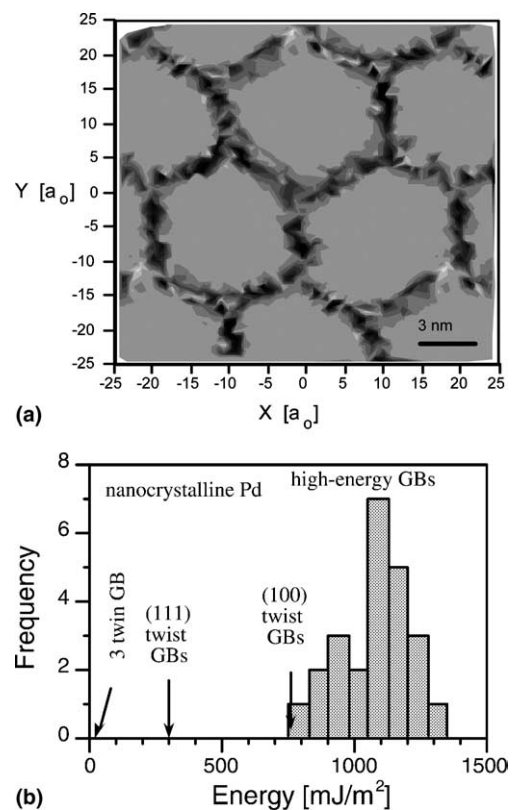


Fig. 4. (a) Energy-per-atom gray-scale contour plot for a (1 1 1) slice through an fcc Pd microstructure that contains the centers of all four grains of uniform grain shape and size. Dark regions indicate high excess energy. (Periodic images of some of the grains are also shown.) (b) Histogram of GB energies obtained for the 24 GBs in the microstructure in (a); the energies of the bicrystalline GBs whose radial distribution functions are shown in Fig. 1 are also indicated [50].

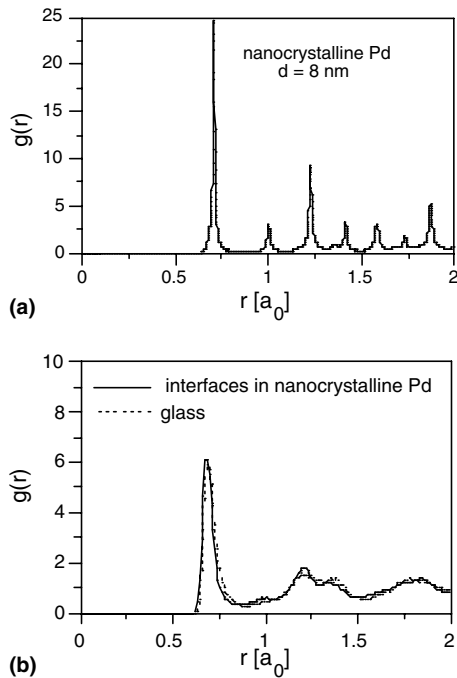


Fig. 5. (a) System-averaged radial distribution function for a Pd microstructure with a grain size of 8 nm (see also Fig. 3(a)). (b) Local radial distribution function for the GB atoms; similar distributions were obtained for the atoms located in the line and point grain junctions. For comparison, $g(r)$ for the bulk Pd glass is also shown [50].

non-vanishing background between the peaks indicates the presence of structural disorder. To elucidate the origin of this non-crystalline signal, the *local* radial distribution functions associated with the GBs, triple lines and point junctions were determined by considering only those atoms in the system with the highest excess energies. According to Fig. 5(b), these local distribution functions reveal a complete absence of long-range order in the highly disordered GBs. In particular, the second crystalline peak has almost completely disappeared. Remarkably, this distribution function is virtually indistinguishable from the radial distribution function of the bulk Pd glass (dashed line; cf. Fig. 1).

A comparison of Fig. 5(b) with Fig. 1(c) reveals that the GBs in the nanocrystalline microstructure have a structure that is virtually identical to that of the high-angle (110) twist GB in Fig. 1(c), i.e., to the universal structure of the high-energy GBs in coarse-grained Pd. The fact that, with an energy of 1025 mJ/m² the (110) GB is, indeed, representative of the high-energy GBs in the nanocrystalline material is supported by the histogram of GB energies in the nanocrystalline microstructure (see Fig. 4(b)). The narrow spread of GB energies, with none of the 24 GBs in the system having an energy lower than 800 mJ/m² or higher than 1300 mJ/m², originates from the random grain misorientations that give rise to GBs having both tilt and twist components, thus effectively inhibiting the formation of low-angle and

“special” low-energy GBs. There is, however, no reason to assume that low-angle and special low-energy GBs do not exist in real materials, in which the misorientations between neighboring grains may not be random.

In summary, the simulation results for Si and Pd suggest that, in the spirit of Rosenhain’s historic “amorphous-cement” model [56–58], the more or less randomly oriented grains in a nanocrystalline, fcc-metal microstructure are connected by a glassy, intergranular, glue-like “phase”. In practice, this intergranular amorphous phase is disrupted by more ordered dislocation boundaries and, perhaps, a few special boundaries other than coherent twins. Furthermore, the analysis of the structures of bicrystalline Si and Pd GBs as a function of their energy reveals the presence, *in thermodynamic equilibrium*, of a glassy intergranular structure in the high-energy GBs while the low-energy GBs are crystalline. These results suggest that a nanocrystalline microstructure *with random grain orientations* contains mostly high-energy GBs. These observations are also consistent with simulations of the phonon density of states and of the related free energy [21,59], which demonstrated that below a certain critical grain size (of typically 1.5–2 nm) nanocrystalline microstructures are thermodynamically unstable with respect to the amorphous phase.

2.3. High-temperature grain-boundary structure and behavior

Recent simulations demonstrated that the highly disordered high-energy GBs in Si and Pd undergo a reversible (i.e., thermodynamic-equilibrium) structural and dynamical transition at elevated temperatures. Here, we demonstrate the profound influence that this transition has on high-temperature GB properties, such as GB migration, sliding and diffusion, and hence on the mechanical behavior of nanocrystalline materials. This behavior is particular relevant to nanocrystalline materials because their microstructure contains a rather high fraction of this type of GB.

Many of the earlier simulations of high-temperature GB structure were controversial for a long time in that they predicted “premelting” at the GBs, i.e., GB disordering below the bulk melting point, T_m (for a critical review, see [60]). By contrast with conventional melting, in which the liquid phase nucleates, e.g., at the GBs, premelting implies the existence of a liquid-like GB layer with a width that gradually diverges as $T \rightarrow T_m$, where the GB is completely wetted by the liquid. It was not until the simulations had provided a clearer understanding of the melting process itself [61,62] and of the related superheating limit [62–64], that a clearer picture of high-temperature GB structure started to emerge.

This picture suggests that upon heating from 0 K to melting, the high-angle, high-energy GBs in the polycrystal undergo a reversible structural and dynamical

transition from a low-temperature, solid GB structure to a mixed solid and liquid, *highly confined* high-temperature GB structure [65]. Remarkably, these simulations revealed that above a certain transition temperature, T_c , which depends on the GB energy, small bubbles of liquid are formed within the highly disordered, solid GB until, at T_m , the liquid bubbles fill the entire – still highly confined – GB region [54]. Finally, for $T > T_m$, the highly confined liquid GB layer spreads to induce thermodynamic melting [61–63]. This *continuous, reversible* transition between T_c and T_m profoundly affects the high-temperature properties of each of these GBs [66]; it is also largely responsible for the rate-controlling role that these GBs play in the evolution of polycrystalline microstructures under the driving forces of stress and temperature.

2.3.1. Grain-boundary migration and diffusion in bicrystals

Recent MD simulations of GB migration [66] and GB diffusion by Schoenfelder et al. [67] in a (0 0 1) $\phi = 43.60^\circ$ ($\Sigma 29$) twist bicrystal in Cu provided clear evidence for the existence of such a GB structural and dynamical transition at elevated temperatures. As seen in Fig. 6(a) and (b), above about $T \sim 750$ K (or $\sim 0.62T_m$ for this Lennard-Jones potential) the activa-

tion energies for both GB processes decrease significantly from their low-temperature values [66]. Detailed analysis exposed a related change in the underlying mechanisms, from a low-temperature mechanism involving solid-like atom hopping to a high-temperature mechanism involving the liquid-like reshuffling of the GB atoms [66,67].

Consistent with these observations of a partially liquid high-temperature GB structure, half a century earlier Mott [68] had suggested that the mechanism for GB migration involves local disordering, or “melting”, of small groups of atoms at the boundary, thereby enabling atoms belonging to one grain to reshuffle collectively while aligning themselves with the opposite grain. According to Mott’s idea the activation energy for GB migration, $Q = nH_f$, should be governed by the latent heat of fusion, H_f , and the average number of atoms, n , involved in the local melting and subsequent reshuffling. To test this idea, Schoenfelder et al. [66] determined H_f by MD simulation; the value of $H_f = 0.13$ eV/atom thus obtained is remarkably close to the experimental value of 0.135 eV for Cu. This value is, indeed, lower than the activation energy for GB migration, $E_{\text{mig}} = 0.20$ eV, in the high-temperature regime in Fig. 6(a), yielding a value of $n = Q/H_f \approx 2$ that is consistent with Mott’s idea. (The fact that in a pure material the activation energies for GB migration and GB diffusion are of rather different magnitude (compare Fig. 6(a) and (b)) indicates that in a pure material the two processes involve different activation barriers and, hence, different atomic-level mechanisms [66].)

To further investigate the possible existence of a crossover from a solid low-temperature to a liquid-like high-temperature GB structure, Keblinski et al. [54] performed extensive simulations of self-diffusion in several carefully chosen high-energy tilt and twist GBs in Pd. The Arrhenius plots thus obtained for four different high-energy GBs (two tilt and two twist GBs) are shown in Fig. 7. Consistent with the GB diffusion experiments of Budke et al. [69] (for details, see Section 2.5), these results strongly suggest that a GB structural transition does indeed take place in these GBs.

As clearly seen from Fig. 7, as a consequence of the GB structural transition the two tilt boundaries undergo a dynamical transition manifesting itself in the crossover in the diffusion behavior, at some transition temperature T_c , from a high-temperature regime with a relatively low, universal activation energy of 0.61 eV to a low-temperature regime with a significantly higher activation energy that varies with the GB geometry. The fact that the twist boundaries in Fig. 7 do not show the transition indicates that T_c is lower than 700 K, where the mean-square displacement of the GB atoms was too small to be detectable in the MD simulations [54].

That, indeed, a structural transition takes place, for example, in the (1 1 0) $\Sigma 11$ twist GB somewhere between

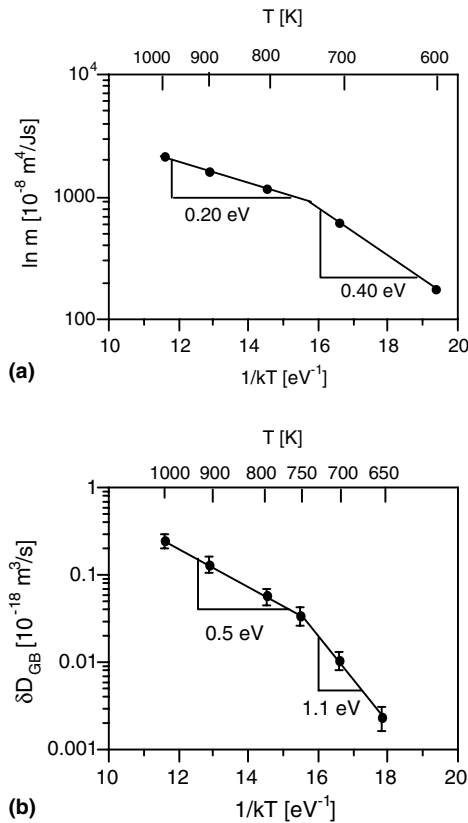


Fig. 6. Arrhenius plots for (a) the GB mobility, m (in units of $10^{-8} \text{ m}^4/\text{Js}$) and (b) the GB diffusivity, δD_{GB} for the (0 0 1) $\phi = 43.60^\circ$ ($\Sigma 29$) twist GB in Cu as described by a Lennard-Jones potential [67].

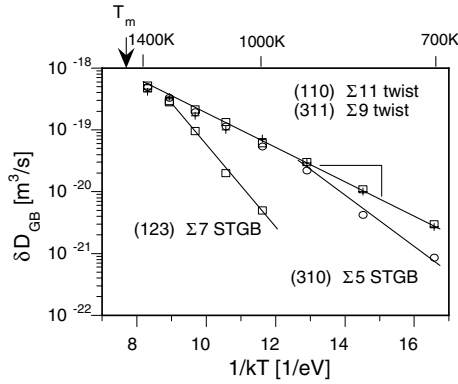


Fig. 7. Arrhenius plots for the diffusion flux, $D_{GB} \delta_D$, between 700 and 1400 K for all four Pd GBs considered in [54]. The melting point for the Pd (EAM) potential used for these simulations was estimated at about $T_m \sim 1500$ K.

1400 and 0 K is seen from the comparison of the radial distribution functions in Fig. 8 and 1(c) [54]. Exhibiting the familiar split second peak, the 0 K structure in Fig. 1(c) is virtually indistinguishable from that of the bulk glass; by contrast, in the high-temperature structure in Fig. 8 this splitting has disappeared and the structure is practically the same as that of the bulk, supercooled melt. A detailed analysis of the jump vectors of the diffusing atoms in the symmetric tilt GB on the (1 2 3) plane (see Fig. 7) provided direct evidence for a crossover in the underlying diffusion mechanism, from a low-temperature mechanism involving jumps in discrete crystallographic directions to an isotropic liquid-like high-temperature mechanism [54].

We finally mention that, in qualitative agreement with an earlier GB diffusion study in Si, the comparison of Pd GB diffusion in the high-temperature regime in Fig. 7 with self-diffusion in the supercooled Pd melt

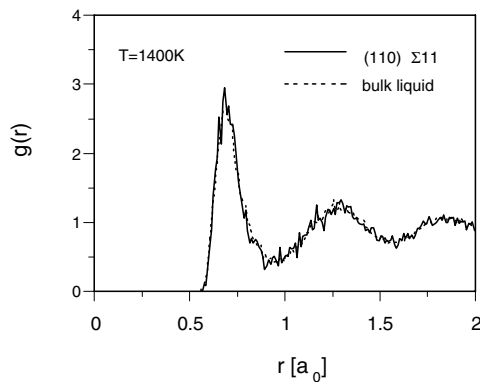


Fig. 8. High-temperature radial distribution function for the atoms in the two central planes of the (1 1 0) $\phi = 50.48^\circ$ ($\Sigma 11$) twist GB in Pd at $T = 1400$ K compared to that of the bulk melt supercooled to the same temperature. The zero-temperature structure of this GB is shown in Fig. 1(c) [54].

demonstrated that the universal activation energy for GB diffusion (of $E_{GB} = 0.60 \pm 0.05$ eV for Pd) is distinctly higher than that in the melt (of $E_{melt} = 0.40 \pm 0.03$ eV for Pd) [54]. It is also worth noting that this value of E_{GB} amounts to only about 25% of that for self-diffusion via monovacancies in bulk perfect-crystal Pd (with a simulated activation energy of 2.41 eV [70]).

The larger picture that emerges from these bicrystal simulations suggests that above a critical temperature T_c , the highest-energy tilt and twist GBs in a polycrystalline material undergo a continuous, reversible transition from a low-temperature, solid GB structure to a highly confined, liquid-like high-temperature structure consisting of liquid bubbles embedded in the solid GB region. As the melting point is reached, the entire GB region is consumed by the liquid bubbles until, above T_m , the highly confined liquid GB layer spreads to induce thermodynamic melting [61–63]. The value of T_c where this structural and dynamical transition occurs increases with decreasing GB energy, with the consequence that the highest-energy GBs in the polycrystal play a rate-controlling role in high-temperature properties, such as grain growth and GB diffusion creep.

2.3.2. Grain-boundary diffusion creep in nanocrystalline Pd

If the structure and properties of the high-energy GBs in a nanocrystalline microstructure are, indeed, identical to high-energy *bicrystalline* GBs, the simulation of GB diffusion creep in the idealized microstructures considered in Section 2.2 (see, e.g., Fig. 4) should provide an important test case. From experimental studies of coarse-grained polycrystals it is well known that Coble creep involves homogeneous grain elongation via GB diffusion, with a creep rate that is linear in the stress, proportional to d^{-3} , and governed by the activation energy of GB diffusion [38]. Due to this d^{-3} increase of the strain rate with decreasing grain size, d , Coble creep should be observable in nanocrystalline materials even during the short observation window of $\sim 10^{-9}$ s typically accessible by MD simulation.

To test the GB structural model described above, MD simulations of 3d periodic nanocrystalline Si [37] and Pd [71] microstructures were performed. To enable steady-state diffusion creep to be observed unencumbered by grain growth, model microstructures were tailored to have a uniform grain size and shape, with random grain orientations. As further described in Section 4.2, these microstructures, indeed, exhibited steady-state diffusion creep that is homogenous, linear in the stress, and with a strain rate that agrees quantitatively with the Coble-creep formula [38].

Most importantly, the temperature dependence of the creep rates thus obtained, for example, in Pd between 900 and 1300 K yielded an activation energy of

0.61 ± 0.04 eV, in remarkable agreement with the universal high-temperature activation energy of 0.60 ± 0.05 eV found for GB diffusion in high-angle, high-energy Pd bicrystals (see Fig. 7). Moreover, for grain sizes larger than about 7 nm, the simulated grain-size dependence obeyed the d^{-3} dependence predicted by the Coble-creep formula [38]. (For further details, see Section 4.2.)

2.4. Grain-boundary structural model for nanocrystalline materials

The significant body of atomic-level simulations described above suggests important similarities and some differences between the GBs in coarse-grained polycrystalline microstructures and nanocrystalline microstructures. The most important differences seem to arise from the severe microstructural constraints present in nanocrystalline materials. As indicated by the highly disordered structure of the coherent twin boundary in Fig. 2, these constraints can have the effect of converting what would otherwise be a “special” (i.e., dislocation-free, low-energy) GB into a highly disordered, high-energy interface. However, as evidenced by the observation in nanocrystalline Pd of perfectly ordered coherent twins transecting the grain interiors [50], the structures of “special” boundaries in a nanocrystalline microstructure may not be unique, but rather may depend on the nature of the microstructural confinement locally at the GB, and hence on the synthesis conditions and the degree of “thermal relaxation” of the material following its synthesis (see also Section 2.5 below).

Therefore, while nanocrystalline and coarse-grained polycrystalline microstructures appear to contain the same three types of GBs (see Section 2.1), the most important measure of their differences probably lies in their GB-energy distribution functions. Whereas coarse-grained materials usually exhibit a broad distribution of GB energies, the severe microstructural constraints present in nanocrystalline microstructures seem to have the effect of significantly increasing the fraction of high-energy GBs at the expense of the special boundaries: The more severe the microstructural constraints become (e.g., by decreasing the grain size or by the use of a highly non-equilibrium synthesis route), the larger appears to be the fraction of the high-energy boundaries in the system. Valiev and coworkers [72,73] have clearly demonstrated that in nanocrystalline metallic materials produced by severe plastic deformation, one observes highly non-equilibrium, high-angle GBs with a structure that facilitates significant GB sliding in the context of nanocrystalline superplasticity. Since, due to their high mobility and diffusivity coupled with a low sliding resistance and high GB energy, these boundaries dominate the evolution of these microstructures in response to stress and temperature, their effect

should be particularly pronounced in nanocrystalline materials.

The above simulations also suggest an intriguing structural and thermodynamic relation between nanocrystalline materials and bulk amorphous solids. Although the high-angle, high-energy GBs represent only a (synthesis and processing dependent) fraction of the GBs in a nanocrystalline microstructure, their structure and behavior strongly resembles Rosenhain’s historic “amorphous-cement” model [56–58]. In fact, in the (hypothetical) limit in which all GBs in a nanocrystalline material are of this type, the two-phase microstructure consists of crystalline grains embedded in a glassy, intergranular, glue-like phase. In practice, this intergranular amorphous phase is disrupted by more inhomogeneously disordered dislocation boundaries and, perhaps, a few special boundaries. Given that in bicrystals this amorphous intergranular phase seems to be of thermodynamic, rather than purely kinetic origin, it appears that a rather intimate relation exists between nanocrystalline microstructures and the bulk amorphous phase. This idea of a thermodynamic connection is further supported by the simulations which revealed the existence of a minimum grain size (of typically 1.5–2 nm) below which a nanocrystalline microstructure is thermodynamically unstable with respect to the bulk amorphous solid [21,59].

2.5. Comparison with experiments

We now discuss the results of experimental work on the atomic structure of GBs in nanocrystalline materials in the context of the above simulation results. Three rather complementary structural characterization tools have been used: X-ray diffraction (XRD), high-resolution transmission electron microscopy (HRTEM) and extended X-ray absorption fine-structure (EXAFS). XRD provides a measure of the radial distribution function of the nanocrystalline material, i.e., a measure of the degree of long-range and short-range structural disorder in the material. Indeed, due to the large volume fraction of GBs in nanocrystalline materials, the XRD signal observed from nanocrystalline materials should consist of two distinct contributions, one from the grain interiors and the other from the GBs and grain junctions. The quantitative evaluation of these signals can provide information about the atomic structure of both the grains and the GBs. By contrast, HRTEM provides a direct atomic-level image of a small area of the microstructure, enabling local structural characterization. While XRD and HRTEM directly probe the atomic-level structure, EXAFS probes the electronic structure from which structural information can be inferred. A key problem in interpreting all of the following structural data lies in the difficulty of reproducibly synthesizing and fully characterizing nanocrystalline materials.

In an early study of inert-gas condensed nanocrystalline Fe exposed to air, Zhu et al. [17] found a strong diffuse background in the X-ray scattering intensity between the Bragg reflections, indicating the presence of significant structural disorder in the system. In a numerical simulation matched to the scattering data, the three outer atomic layers of each crystallite were found to be disordered, with random atomic displacements of 50% of the nn distance. A rather different structural picture emerged from a later high-vacuum study of nanocrystalline Fe [74], which exhibited a much lower X-ray diffuse intensity, i.e., much less GB structural disorder. Moreover, an X-ray investigation of nanocrystalline Pd (which is less prone to oxidation than Fe) did not reveal an increase in the diffuse background [75], a finding which was interpreted in terms of rather ordered GB structures.

That these two rather different conclusions are not necessarily inconsistent with one-another is suggested by studies showing that the GB structure of nanocrystalline materials can depend strongly on their processing history. For example, Löffler and Weissmüller [76] studied the atomic structure of the GBs in nanocrystalline Pd prepared by inert-gas condensation, however under a number of different consolidation, aging and annealing conditions. From analysis of XRD data, they found that that the number of nearest neighbors in the crystal-lattice coordination shells depends on the time-temperature history of the sample. In particular, in samples examined within 10 days of preparation, about 10% of the atoms were found to be located on non-lattice sites, corresponding to about two atomic layers of atoms at the GBs on non-lattice sites, i.e., with little or no atomic short-range order. By contrast, in samples aged for several months at room temperature and in samples annealed at elevated temperatures, practically all atoms were found to be located on crystal-lattice sites, with only about one quarter of a monolayer of atoms located on non-lattice sites. Moreover, the distribution of nn interatomic spacings (as probed by the X-ray Debye–Waller parameter) suggested displacements correlated over several lattice parameters, rather than the short-range, uncorrelated atomic displacements present in the fresh samples.

Local structural characterization using HRTEM also provided evidence for both ordered and disordered GB structures. For example, HRTEM studies of nanocrystalline Pd and Cu showed narrow and faceted GBs [77]. However, it is important to recall that HRTEM sample preparation may have a significant effect on GB structure. Most importantly, HRTEM samples have to be thinned to a thickness of the order of one grain diameter or even less, thus eliminating a significant number of the constraints on the GBs. It is well-known that rigid-body translations of the crystallites parallel and perpendicular to the GB plane are essential for minimizing the GB energy [78]. Consistent with this, the above

computer simulations revealed that under the severe constraints imposed by the surrounding crystals in bulk nanocrystalline microstructures, these translations cannot be simultaneously optimized along all the GBs (see, e.g., the highly disordered, high-energy structure of the coherent twin in the lower half of Fig. 2). In necessarily thin HRTEM samples the rigid-body translations can therefore be more readily optimized than in a bulk nanocrystalline material, thereby possibly inducing a relaxation towards more ordered GB structures with lower energies. Moreover, HRTEM imaging requires certain low-index directions of each crystallite to be parallel to the electron beam. As a consequence, only a few rather special tilt boundaries can be imaged with atomic resolution. However, in the absence of the severe microstructural constraints present in a bulk nanocrystalline material, such boundaries are known to be well ordered and to have low energies. In other words, HRTEM yields atomic-resolution structural information only for well-ordered, low-energy boundaries but not for random ones.

In order to avoid some of the difficulties associated with HRTEM sample preparation, recently Ranganaathan et al. [79] determined the atomic structure of GBs and triple junctions in Pd and Ti nanocrystalline thin films produced by physical vapor deposition (PVD). Their observation in both materials of bright contrast at many triple junctions was interpreted as arising from local structural disorder. Moreover, while some of the GBs in their micrographs appeared sharp and well defined, others showed considerable structural disorder. They estimated that the disordered GB region is only about 0.5 nm wide. This estimate agrees remarkably well with the GB widths extracted from the MD simulations of nanocrystalline fcc metals (see, e.g., Figs. 2 and 4) and Si [53] and of high-energy, highly disordered bicrystalline GBs (see, e.g., Fig. 1) [52,54].

Further evidence for the presence of highly disordered GB structures in nanocrystalline metals has come from EXAFS studies, which revealed a strong reduction in the nn coordination number in Cu and Pd [18] as well as other fcc and bcc metals [76,79]. These experiments also provided evidence that the GB structure changes with room-temperature aging and annealing [80]. In agreement with the structural information deduced from XRD on nanocrystalline Pd described above [18], this relaxation results in a more ordered GB structure in which the atoms are situated close to lattice sites of either of the two grains forming the GB.

In summary, the above ambient-temperature XRD and EXAFS studies on nanocrystalline *metals* indicate that (i) the atomic structure of the GBs depends on the preparation procedure and on the presence of impurities, and (ii) the structure of well-relaxed GBs is similar to the structure of microstructurally unconfined bicrystalline GBs.

Similar studies on *covalent* materials have been performed so far primarily for Si. Shen et al. [81] demonstrated by XRD that ball milling of Si can be used to produce a two-phase, nanocrystalline and amorphous microstructure; for an average grain size of 8 nm they found that about 15% of the material was amorphous [81]. Extensive earlier Raman-spectroscopy work on nanocrystalline silicon [82] had also identified a strongly grain-size dependent amorphous component, with an atomic structure that was virtually indistinguishable from amorphous Si. Similar evidence obtained for a Ti–Ni alloy deformed by severe torsional plastic deformation at room temperature and high (7 GPa) pressure, yielded a mixture of approximately 5 nm Ti–Ni nanocrystals (~20% of the sample) embedded in an amorphous matrix of Ti–Ni as observed by TEM [83]. These results agree well with the structural picture that has emerged from the MD simulation on Si and Pd (see Section 2.2). However, it should be noted that an inherent limitation of the experimental studies is the difficulty in determining the location and spatial distribution of the amorphous component within these highly inhomogeneous microstructures, i.e., to answer the question as to whether entire grains are amorphous or whether perhaps only the GBs and grain junctions are highly disordered.

Measurements of H diffusivity and solubility provide another approach towards elucidating the ambient-temperature atomic structure of nanocrystalline materials [84]. H atoms can enter interstitially into both the GB regions and the crystalline grains. Whereas in the crystalline regions the H sites are characterized by discrete energy levels, the interfacial sites exhibit a distribution of site energies; this distribution contains information on the boundary structure and may be compared with the H site-energy distribution in metallic glasses. This idea was applied by Kirchheim [84] to compare the atomic structure of nanocrystalline Pd with the structures of amorphous Pd–Si and Ni–Ti alloys. The observations on nanocrystalline Pd revealed a Gaussian function for the site energies in the GB regions and a Dirac δ function for the grain interiors. Moreover, the width of the Gaussians obtained for the GBs was found to lie between those obtained for two different amorphous Pd–Si alloys, formed by melt spinning and sputtering, respectively. These observations are in qualitative agreement with the radial distribution functions for the GB-core structure extracted from the MD simulations (see, e.g., Fig. 5(a)).

Let us now move on to the temperature dependence of GB structure in nanocrystalline materials obtained, e.g., from the study of GB diffusion. For example, Würschum et al. [85] used diffusion measurements to compare the atomic structures of the GBs in coarse-grained and nanocrystalline polycrystals with the structure of glasses with the same chemical composition. On

the one hand, their observation of similar radiotracer diffusion coefficients in pure, highly densified nanocrystalline Pd measured at temperatures between 371 and 523 K and in coarse-grained polycrystals suggests similar GB structures, i.e., independent of the grain size. Given the effects of annealing on the structure of GBs in nanocrystalline materials described above, this observation is not very surprising. On the other hand, however, the diffusivity of ^{59}Fe in crystallized $\text{Fe}_{73.5}\text{Si}_{13.5}\text{B}_9\text{Nb}_3\text{Cu}_1$ (FINEMET) with a grain size of ~13 nm was found to be higher than in the amorphous alloy with the same chemical composition, suggesting a rather open GB structure in the nanocrystalline material by comparison with the glass of the same composition.

Recent self- and impurity-diffusion experiments [69,86] on Cu $\langle 001 \rangle$ tilt GBs near the $\Sigma 5$ (36.87°) misorientation revealed a crossover from a low-temperature diffusion mechanism with a high activation energy to a “universal” high-temperature mechanism with a much lower activation energy. These measurements on carefully characterized bicrystals (see Fig. 9 for Au diffusion in Cu bicrystals) yielded the same, misorientation-independent and rather low *high-temperature* activation energy; by contrast, below the transition temperature, the activation energy was found to be significantly higher and strongly dependent on the GB misorientation. This transition was interpreted as a GB structural transition, from an ordered low-temperature GB structure to a disordered high-temperature structure with randomly directed jump vectors. This interpretation is consistent with the simulations of self-diffusion in high-energy GBs of Pd described in Section 2.3 (see Figs. 6–8), revealing a GB structural transition on

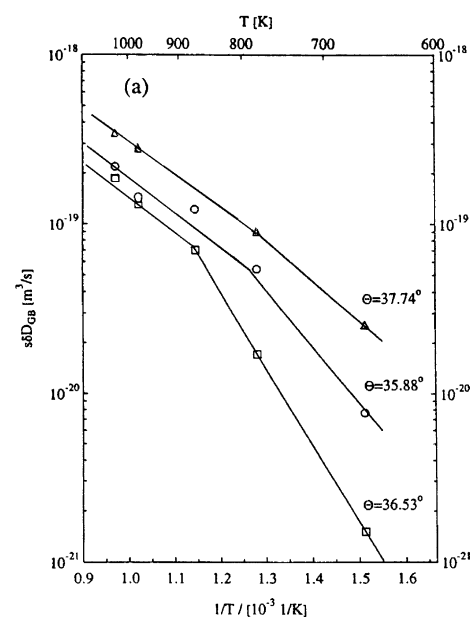


Fig. 9. Arrhenius plots for Au diffusion along $[001]$ tilt GBs in Cu near the $\Sigma = 5$ misorientation of $\theta = 36.87^\circ$ [69,86].

heating, from a highly disordered, solid low-temperature GB structure to a liquid-like high-temperature structure. A similar GB structural and dynamical transition was observed in MD simulations of high-energy Si bicrystals [65], revealing that the transition is a thermodynamics-based equilibrium transition (i.e., fully reversible) and related to the glass transition, however modified by the confinement of the amorphous GB phase by the delimiting grains.

Another investigation of high-temperature GB structure involved a model system consisting of thin films of Ga confined between two Al_2O_3 crystals of different crystallographic orientations; Ga and Al_2O_3 do not react chemically [85,87]. The thickness of the Ga films could be controlled by the volume fraction of Ga at any given Al_2O_3 grain size. Film thicknesses from less than a monolayer up to about 10 monolayers of Ga were studied. The atomic structure and mobility of the confined Ga films were investigated by X-ray diffraction, differential scanning calorimetry and quasielastic neutron scattering between 17 and 320 K (the melting point of Ga) [85,87]. The results thus obtained may be summarized as follows. If the Ga films were six monolayers or less thick, they remained amorphous at all temperatures, although Ga crystallizes below 303 K. The mobility of the Ga atoms at temperatures close to about 300 K was comparable to that in liquid Ga. The temperature variation of the X-ray diffraction pattern of the Ga films revealed a continuous, reversible structural transition. Consistent with the MD simulations described in Section 2.3, these observations suggest that (i) at temperatures close to the melting point, the atomic mobility in the GBs is comparable to the mobility in the supercooled melt, and (ii) decreasing the temperature induces a GB structural transition that reduces the atom mobility to values comparable to those observed in GBs in coarse-grained materials or glasses.

In summary, the experiments reviewed above support two key findings of the MD simulations. First, the disordered atomic structures of highly constrained high-angle GBs in nanocrystalline materials appear to be not fundamentally different from those of entirely unconstrained high-energy bicrystalline GBs. Second, the structures of these boundaries seem to be rather similar to bulk amorphous structures. It is also clear, however, that sample processing history has a strong effect on the types of structures detected, and more work is clearly needed to elucidate this relation.

2.6. Critical issues and outstanding questions

Rigorous tests of the results of the MD simulations obviously require experiments that are designed to measure the computed structural parameters under well-controlled conditions. Si seems to be one of the best model systems for such a test, involving, e.g., XRD

experiments on thin-film bicrystals prepared under UHV conditions and of nanocrystalline Si as a function of temperature and grain size. Measurements of this type would be of general relevance because they appear to be capable of providing a critical test for the applicability and limitations of the MD simulations. Most interaction potentials available for Si capture the crystalline, the liquid and the amorphous structure of Si without adjustable parameters. Hence any discrepancies noted between well-designed model experiments and the corresponding simulations would be extremely useful towards elucidating the validity and limitations of the MD results.

3. Dislocation plasticity for larger grain sizes and existence of d_c

The common low-temperature plastic-deformation mechanism in coarse-grained metals and ceramics involves the continuous nucleation of dislocations from Frank–Read sources and their glide through the crystal on well-defined slip systems. In a polycrystalline material the size of these sources cannot exceed the grain size. Since the stress needed for their operation is inversely proportional to the size of the source, this deformation mechanism can operate only down to a grain size of typically about 1 μm . For smaller grain sizes, mobile dislocations must be nucleated from other sources, such as the GBs or grain junctions. In this section, we review recent MD simulations of columnar nanocrystalline-Al microstructures [25,26,71] which revealed the existence of a length-scale competition between the grain size and the dislocation splitting distance; this competition renders dislocation processes less and less effective until, at a critical grain diameter, d_c , GB-based deformation processes take over. These simulations also revealed a propensity for deformation twinning and subsequent strain hardening.

3.1. Columnar simulation model for Al

Yamakov et al. [25] determined the behavior of $\langle 110 \rangle$ -textured microstructures consisting of four grains of identical size and a regular-hexagonal shape in the simulation cell. These microstructures have the advantage over fully 3d microstructures that a considerably larger grain size can be considered. As illustrated in Fig. 10 the four grains in the 3d periodically repeated simulation cell are oriented relative to the tensile (x) axis by rotations about $[110]$ by the angles 0° , 30° , 60° and 90° . The 12 high-angle GBs in the system therefore consist of three groups of identical asymmetric $[110]$ tilt GBs: whereas the 30° and 90° boundaries are high-energy GBs, with a highly disordered atomic structure [43,51,52,54], the

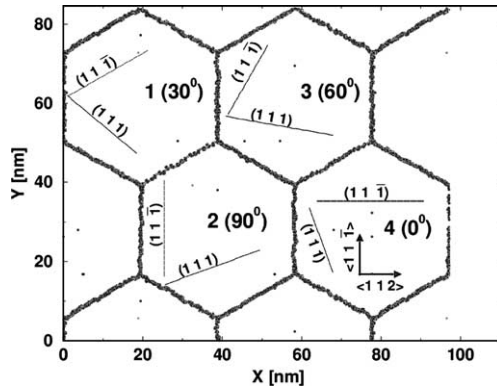


Fig. 10. Orientations of the four grains relative to the edge of the simulation cell (X -direction, corresponding to the $\langle 112 \rangle$ direction in grain 4; i.e., the misorientation angle of each grain is given by the angle between its $\langle 112 \rangle$ direction and the X axis). The orientations are mapped onto a $[110]$ -projected snapshot of the system with a grain size of $d = 45$ nm after its thermal equilibration at $T = 300$ K but prior to application of external stress. Also indicated are the orientations of the two sets of $\{111\}$ slip planes in each grain. Only atoms with nn coordination deviating from the fcc perfect-crystal value of 12 are shown. The continuous network of these miscoordinated atoms tracing the GBs indicates that all these $[110]$ tilt GBs are high-angle GBs. The GBs remain perfectly straight until the threshold stress for the nucleation of dislocations is reached [71].

60° tilt GBs have a dislocation structure because their misorientation is vicinal to the $\Sigma = 3$, 70.53° tilt misorientation. The $\langle 110 \rangle$ column axis (z -direction) ensures that, following their nucleation, dislocations can glide on either of two $\{111\}$ slip planes, activating six slip systems in each grain (out of the 12 that are possible in a fully 3d microstructure), unimpeded by the 3d periodic border conditions imposed on the simulation cell.

The minimum thickness of the simulation cell in the columnar (z) direction is determined by the cut-off radius, $R_c = 1.37a_0$, of the EAM potential for Al of Ercolessi and Adams [88] used for the simulations. This potential yields a zero-temperature lattice parameter $a_0 = 4.03$ Å. The simulation cell contains only 5 periodically repeated (110) planes (or 10 (220) planes, giving a simulation-cell thickness of $\sim 3.5a_0$ in the z -direction), the net effect being that any dislocations nucleated from the GBs are constrained to being straight lines. By contrast with the z -direction, the simulation-cell size in the x - y plane is determined solely by the grain size, d ; for values ranging between $d = 20$ and 100 nm, the simulated systems thus contained between 97,000 and 2,425,000 atoms. The potential was slightly modified for a higher degree of smoothness at the cut-off radius; this modification increases the stacking-fault energy from 104 to 122 mJ/m², i.e., closer to the experimental values, ranging between 120 and 142 mJ/m² [89].

All simulations were carried out under constant tensile loads of 2.3–2.5 GPa and at a temperature of $T = 300$ K. Ercolessi and Adams [88] estimated the melt-

ing point for this potential at 940 K, compared to the experimental value of 933 K. For further details, see [25].

3.2. Length-scale effects in the nucleation of dislocations from the grain boundaries and existence of d_c

The most common dislocations responsible for the slip deformation of fcc metals are extended dislocations, their cores being split into two Shockley partials connected by a stacking fault. The length of the stacking fault, i.e., the dislocation splitting distance, r , depends on the stacking-fault energy, Γ , and the resolved shear stress, σ , on the glide plane as [90].

$$r = K_1 b^2 / (\Gamma - K_2 \sigma), \quad (1)$$

where $b = a_0/\sqrt{6}$ is the length of the Burgers vector of the partials; K_1 and K_2 are numerical factors depending on the elastic constants of the material and the types of partials forming the extended dislocation. Under the high stress required to nucleate dislocations from the GBs, the magnitude of r can be significant and, for a nanocrystalline grain size become comparable to, or even larger than, d . Thus r introduces a new length scale into the problem in addition to d , because a complete extended dislocation cannot be nucleated unless $d > r(\sigma)$ (cf. Fig. 11(a) and (b)). (The full process of nucleation can be seen in *Video 1* in the supplementary material to this paper.)

The requirement that $d > r(\sigma)$ represents a necessary condition for the dislocation-glide mechanism to be fully operational. When d becomes comparable to r (see Fig. 11(a)), only single partials can be nucleated, producing stacking faults in their glide through the grains. This regime has been considered previously for nanocrystalline Ni and Cu [23,91–94], with the same result. The interplay between $r(\sigma)$ and d thus results in a grain size below which the slip process becomes less and less effective in producing plastic strain and the GB based deformation starts to dominate. This suggests that a critical grain size, $d_c \sim r$, exists below which the material starts to soften due to the domination of a GB based deformation mechanism. However, as discussed in Section 5.2, the grain-size dependence of the dislocation-nucleation stress also enters into d_c .

An interesting observation is that when the applied stress is turned off, any previously nucleated dislocation (see Fig. 11(b)) tends to get re-absorbed reversibly by the GB at the same place from which it was nucleated [25]. (One such event is captured in *Video 2* in the supplementary material.) The initial dislocation-free structure is thus restored, provided the plastic strain was small enough that no dislocation reactions or entanglements had taken place. This plastic reversibility suggests that, in agreement with experimental observations (see Section 3.4), at this extremely small grain size the grains

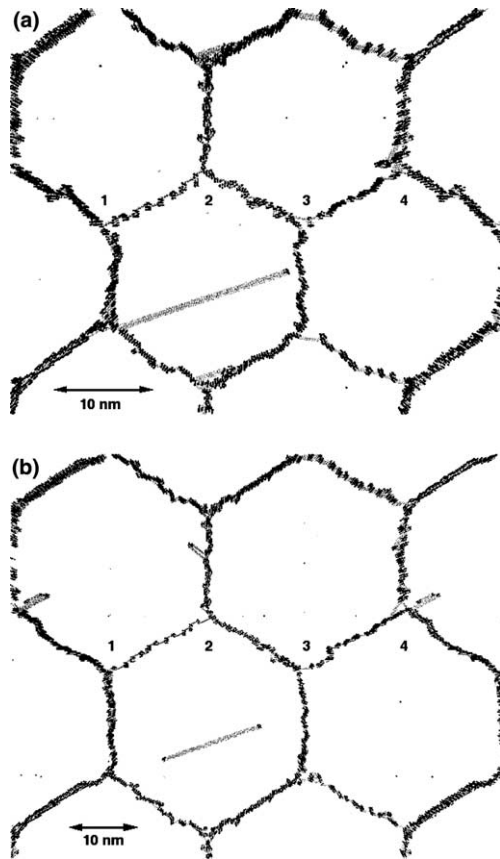


Fig. 11. (a) Snapshot of the $d=20$ nm system at 14.6 ps of deformation time; a nucleated partial $1/6[1\ 1\ 2]$ dislocation is observed, leaving behind an intrinsic stacking fault. (b) Snapshot of a crystallographically identical system, however with a 30 nm grain size, at 27.6 ps of deformation time. A fully developed extended $1/2[0\ 1\ 1]$ dislocation dissociated into two partials is observed. In both snapshots the applied tensile stress is 2.3 GPa; however, the average internal stress in grains 2 and 4 is 2.77 GPa [25]. Here and throughout, common-neighbor analysis was used to identify perfect-crystal atoms as being either in a local hcp (gray atoms) or fcc environment (atoms not shown). Black atoms are “defected”, i.e., neither in an fcc nor hcp environment, including atoms not having 12 nearest neighbors. (The full process of nucleation can be seen in *Video 1* in the supplementary material to this paper; *Video 2* in the supplementary material captures the reversible reabsorption of the dislocation in (b) by the same GB and at the same place from which it was nucleated.)

cannot sustain single, mobile dislocations without external stress.

3.3. Deformation twinning in nanocrystalline Al

As the plastic strain increases, the dislocation concentration in the grain interiors continues to increase, giving rise to various types of intragranular dislocation–dislocation interaction processes associated with the glide of extended dislocations on different slip systems. (The entire deformation simulation, out to a plastic strain of $\sim 12\%$, is shown in *Video 3* in the supplementary material.) Most of these processes are well-known from extensive deformation studies in single crystals and

coarse-grained polycrystals [90,95,96]. Among the best known is the formation of Lomer–Cottrell locks [96,97] seen in each of the four grains in Fig. 12.

In addition to these *intragranular* processes, these simulations also reveal a variety of unanticipated and intriguing *intergranular* processes, involving the interaction of dislocations with GBs and deformation twins formed during the simulation [71]. Their net combined effect after $\sim 12\%$ plastic strain is shown in the snapshot in Fig. 12 for a grain size of 45 nm.

The considerable roughness of the initially flat GBs is particularly noticeable (compare with Fig. 10). This roughness arises entirely from dislocation–GB interaction processes, as evidenced by the fact that for a stress slightly below the dislocation-nucleation threshold, the GBs remained perfectly straight during the entire deformation simulation. Moreover, a new grain labeled A has been nucleated at those GBs that were especially active during these emission/absorption/twin-formation events [26]. In addition, Fig. 12 reveals a mechanism for what at first sight appears to be GB splitting (see, e.g., the GB between grains 2 and 3). However, detailed analysis reveals that the ordered deformation substructure in grain 2 arises from a massive emission of Shockley partials trailed by *extrinsic* stacking faults. Interestingly, the cores of the partials are aligned, presumably due to elastic interactions among them; this eventually leads to the formation of a new dislocation boundary [26].

A unique aspect of this work arising from the ability to deform to rather large plastic strains and to consider a relatively large grain size, is the observation of extensive deformation twinning under the very high GB and dislocation densities that can be present in these materials [26,71,98]. In fact, three distinct mechanisms for

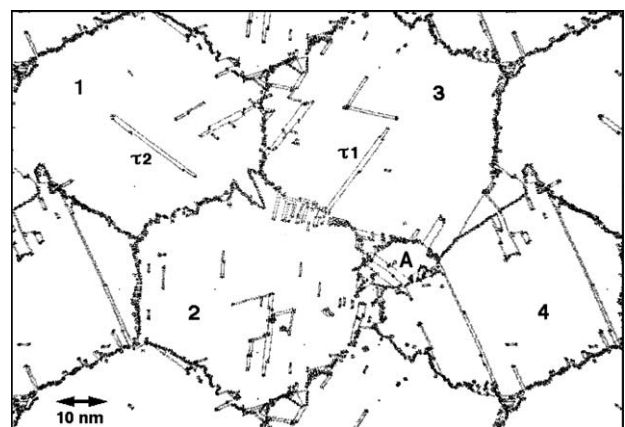


Fig. 12. Snapshot at 11.9% plastic strain for the structure in Fig. 9 ($d=45$ nm) [26]. A variety of processes involving dislocation–dislocation and dislocation–GB interactions are shown to take place. Formations τ_1 and τ_2 in grains 3 and 1 mark two distinct types of deformation twins. Whereas τ_1 was heterogeneously nucleated from the GB, τ_2 was homogeneously formed inside the grain interior via dislocation–dislocation reactions. Formation of a new grain, labeled A, is also seen. (The entire deformation simulation, out to a plastic strain of $\sim 12\%$, is shown in *Video 3* in the supplementary material.)

deformation twinning have been observed (see also Fig. 12). The simulations revealed a high concentration of stacking-fault planes in the grains produced by single partials or by dissociated perfect dislocations. These stacking faults confined by the dense GB network of the nanocrystal were found to initiate deformation twinning, the underlying twinning mechanisms involving partial dislocations and their interaction with the GBs, including stacking-fault overlapping and the coordinated nucleation of partial dislocations from the GBs [71]. In view of the classic understanding of deformation twinning (see e.g., [99]) as a phenomenon limited to relatively large grain size and materials with low stacking-fault energy, such as Cu [100], these observations for nanocrystalline Al are very surprising. Interestingly, however, previous simulations for nanocrystalline Cu had already revealed the emission of *extrinsic* stacking faults from the GBs early during the deformation [91]; however, their coordinated nucleation and propagation across the grain interiors giving rise to deformation twinning during the later stages of the deformation had eluded detection because of the small grain size to which these simulations were limited.

Yamakov et al. [98] suggested that the process of deformation twinning can have a two-fold effect on the mechanical behavior of the material. First, early during the deformation when the grain interiors are practically free of dislocations, it can facilitate the deformation by adding additional slip systems or by facilitating the transfer between existing slip systems through dislocation-twin reactions. Second, once twins have been formed they can repel certain types of gliding dislocations and give rise to pile-ups (see Fig. 13), with consequent strain hardening of the material.

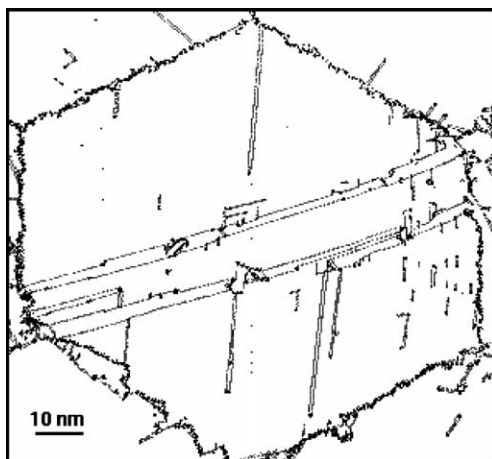


Fig. 13. Grain from the microstructure in Fig. 9 with a grain size of 100 nm at about 10% plastic strain. Dislocation-twin reactions lead to the formation of complex twin networks consisted of twin boundaries on both (1 1 1) and (1 $\bar{1}$ 1) planes, connected by stair-rod dislocations at the crossing points. These networks trap the dislocations to form pile-ups, as can be seen in the right part of the grain; these pile-ups probably give rise to work hardening in our model system [98].

3.4. Comparison with experiments

There is now considerable experimental evidence in support of the intensive dislocation activity in nanocrystalline fcc metals revealed by the MD simulations. Most of the studies presently available on the plastic deformation of micro- and nanocrystalline fcc metals (Au, Ag [82,101–103], Cu [82,104,105] and Pt [82,104], Ni [85,106]) and several fcc alloys [85,107,108] indicate consistently that above a critical grain size of the order of 30–100 nm, depending on the metal, dislocations are observed (via direct TEM observations, lattice-fringe rotation, in-situ videotaping, contrast fluctuations) to move across the crystals as perfect dislocations during plastic deformation. In TEM, segments of these dislocations are visible in the interior of the crystals. Below this critical grain size, the dislocations rapidly move across the grains and are absorbed by the boundaries leaving no dislocation segments in their wake.

The importance of partial dislocations and stacking faults or twins in the plastic deformation of nanocrystalline fcc metals has recently been addressed by several authors. Markmann et al. [109] used XRD and TEM to follow the microstructural evolution during deformation of Pd samples with a grain size in the 10–30 nm range consolidated from clusters by cold-rolling at different deformation rates (between 10^{-10} and 10^{-3} s $^{-1}$). A strong increase in stacking-fault density was noted when the specimens were deformed at high strain rates. Fig. 14 compares the development of the stacking-fault parameter [110], α_{Warren} , during the rolling cycles of nanocrystalline Pd with a grain size of $d = 28$ nm (open squares) with that for coarse-grained Pd with $d > 100$ nm (solid diamonds). The nanocrystalline sample clearly exhibits a larger maximum value of α_{Warren} and a steeper

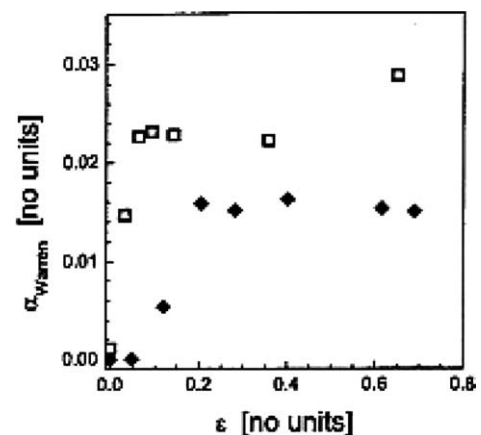


Fig. 14. Stacking-fault parameter, α_{Warren} , vs. the true strain ϵ for nanocrystalline (□) and coarse grained (◆) Pd. X-ray diffractograms were taken from both sides of the sample; α_{Warren} is the arithmetic mean of both values. Figure reproduced from [109].

initial increase [111,112], suggesting that deformation in the nanocrystalline sample occurs predominantly via partial dislocations. Although the values of α_{Warren} do not give quantitative information on the number density of the faults [113], the observation provides conclusive evidence for a substantial increase in stacking-fault density during deformation of both samples, suggesting that partial dislocations and/or twinning must be active in nanocrystalline Pd, at least during the initial stage of the deformation.

Some of the key predictions from the columnar-model simulations by Yamakov et al. [25,26,71,98] have gained solid experimental support. Among these is the observation in nc Al of the nucleation of perfect dislocations by the successive emission from the GBs of leading and trailing Shockley partial dislocations, resulting in a transition with increasing grain size from partial-dislocation slip to the conventional slip mechanism [114]. Several TEM studies on the deformation mode in pure nanocrystalline Al [27,115], Al–7.5 wt% Mg [115,116] and Al–7.6 wt% Mg [117] at different grain sizes revealed that below a critical grain size of the order of 10–20 nm, deformation twinning becomes an important deformation mode, even if deformation twinning has never been seen in coarse-grained samples with nominally high stacking-fault energy. Similar findings have been reported for other fcc metals, such as Cu [118,119], Ni [120] and Pd [121]. Moreover, direct TEM observation by Liao et al. in nc Al confirmed the existence of all three twinning mechanisms observed in the simulations [71], namely via stacking-fault overlapping in the grain interiors [122], coordinated nucleation of partial dislocations from the GBs [117], recently also found in nc Cu [119], and GB splitting [122].

Taking advantage of the inherently highly non-uniform deformation during high-pressure torsion, in a recent study Liao et al. [123] used severe plastic deformation to produce three regions with vastly different grain sizes (ranging from about 200–10 nm) and with varying grain shapes (elongated vs. equiaxed) and deformation histories in the same copper sample. This approach thus avoided the problems of comparing the mechanical behavior in samples with different deformation histories, enabling TEM deformation studies for grain sizes ranging from the submicron range down to the nm range under identical deformation conditions. A detailed analysis of the TEM images obtained in the three regions demonstrated that different deformation mechanisms dominate in each. Specifically, the regions with the smallest grain sizes contained a considerably higher dislocation density combined with extensive deformation twins; the latter were formed by the mechanism of coordinated partial-dislocation emission from GBs seen in the MD simulations (see, e.g., Figs. 12 and 13). By contrast, in the submicron grain-size region the grain-size effect of twinning could be described by

the conventional pole mechanism known from the study of coarse-grained materials. These experiments thus confirm the predictions based on the MD simulations of distinct new twinning mechanisms operating in nanocrystalline materials [123].

Of particular interest is the report by Rösner et al. [121] of similar deformation-twinning processes in another high-SFE fcc metal, Pd. A comparison between their Al [27] and Pd [121] experiments showed similarities with the MD results in the way the deformation twins were formed. However, in contrast to the MD simulations, in both Pd and Al the twins were found to form on only one slip plane per grain; thus the twins were always coplanar within each grain. As one slip plane is not enough to accommodate a general deformation, an additional deformation mechanism is required. Rösner et al. suggested that grain rotation will allow the grains to orient their active twin plane along the principal shear direction. By contrast, the MD simulations [98] indicated the appearance of twin networks where two twin planes operate on an equal basis. A possible reason for this might be the much higher strain rates in the MD simulations compared to the experimental studies.

Because deformation twinning is not observed in coarse-grained Al, the formation of deformation twins in nanosized grains seems to be directly related to the nanocrystalline microstructure [28]. Regarding the mechanical twinning of fcc metals, several models have been proposed [44] in which deformation twins are created by stacking faults led by $1/6\langle 1\ 1\ 2 \rangle$ Shockley partials. In terms of these models, the preference for twinning in nanocrystalline materials may be understood by comparing the critical shear stress needed to nucleate a perfect ($1/2\langle 1\ 1\ 0 \rangle$) dislocation with the stress required to initiate the Shockley-partial twinning dislocation, assuming the size of the dislocation source to be proportional to the grain size. If the GBs are assumed to act as dislocation sources, as suggested by the MD simulations, the stress required to nucleate a Shockley partial is found [27] to be less than that required for a perfect dislocation, when the grain size becomes smaller than a critical value, d_c . For Al, d_c is estimated to be approximately 10–15 nm. This model implies that deformation twinning occurs when the GBs start to nucleate more partial dislocations than perfect ones. Rösner et al. [121] argued that this condition alone is not enough as they observed that twin nucleation had started at 3 times higher strain rates than that needed for partial dislocation nucleation. Thus, although it may be energetically favorable to nucleate a partial instead of a perfect dislocation, this does not necessarily imply that twinning occurs; an additional condition, such as high strain rate, seems to be required.

In summary, the MD observations of the preferential generation of partial dislocations, resulting in the

formation of stacking faults and deformation twins in nanocrystalline grains [26,71,91,98], are now fully supported by experimental data. Twinning may also offer an alternative interpretation to explain the grain-size strengthening in terms of dislocation pile-ups against the twins [98].

3.5. Critical issues and outstanding questions

All explanations put forward to date for the deformation of nanocrystalline materials by perfect or partial dislocations are based on the assumption that GBs may act as sources for both perfect and partial lattice dislocations. It appears that at small grain sizes, deformation via partial dislocations (which may result in twinning) is preferred due to the smaller line tension of the partials. Although GBs have been known for more than four decades to be able to emit lattice dislocations [124,125], the processes involved have remained poorly understood up to now, because it is difficult to study them with atomic-level resolution. MD simulations of the plastic deformation of polycrystals of realistic sizes seem to open the way to unravel the processes involved in dislocation emission from GBs. Of particular interest is the dependence of the mechanisms for the nucleation of both partial and complete dislocations and the related critical shear stresses that act on the GB structure.

From the experimental results presently available, the predicted correlation between the stacking fault energy and d_c cannot be tested. Hence a systematic study of this kind would provide a critical test for the ideas proposed from the MD simulations. Moreover, recent ambient-temperature observations [75,126,127] seem to suggest perfect elasto-plasticity to exist in nanocrystalline Cu and presumably in other nanocrystalline metals as well. This observation seems not to be born out by the MD simulations and may require further experimental as well as theoretical studies.

The above simulations also suggest that the Hall–Petch hardening observed in many nanocrystalline fcc metals may arise from pile-ups against deformation twins in the grain interiors which block the glide of GB-nucleated lattice dislocations (see Fig. 13), rather than from pile-ups against the GBs themselves. Experimental tests of this prediction are clearly needed.

4. Grain-boundary based deformation mechanisms for the smallest grain sizes ($d < d_c$)

The various simulations performed to date on the deformation behavior for the smallest grain sizes ($d < d_c$) agree in that all suggest that (a) the deformation process is governed by GB-mediated processes and (b) the material should soften with decreasing grain size.

However, the simulations differ with respect to the specific GB mechanism(s) proposed to be responsible for this behavior.

4.1. Simulation of low-temperature deformation

About six years ago, inspired by experimental reports of inverse Hall–Petch behavior below some critical grain size, Schiotz et al. [23,91] and Swygenhoven et al. [24,128] started to simulate low-temperature plastic deformation of fully 3d microstructures containing typically about 10–50 grains with distributions in their shapes and sizes (of less than $d \sim 20$ nm). To render the deformation observable by MD simulation, very high stresses of ~ 1 –3 GPa had to be applied. Similar to the experiments, Schiotz et al. determined the yield stress, σ_Y , as a function of the grain size, whereas Swygenhoven’s team focused on the strain vs. time behavior from which the strain rate and its activation energy can be extracted. Consistent with previous suggestions based on experiments [6,7], both teams identified GB sliding as the dominant deformation mechanism.

The early simulations of Schiotz et al. [23,91] reported mechanical softening of the low-temperature yield stress of nanocrystalline Cu with decreasing grain size (from 6.6 to 3.3 nm). By identifying and visualizing the areas with the most inhomogeneously displaced atoms relative to the overall *homogeneous* deformation in the simulated sample, they presented evidence for the existence of GB sliding combined with grain rotation. In some of the larger grains ($d \geq 5.2$ nm), they also observed the nucleation of partial dislocations from the GBs. Following their nucleation, these incomplete extended dislocations traveled across the grains, leaving behind intrinsic stacking faults.

Using a similar approach for simulations of nanocrystalline Ni with an average grain size of 3.4–5.2 nm at 70 K, Swygenhoven et al. [24,128] showed that under the low-temperature, high-stress conditions in these simulations, GB sliding and grain rotation were the elementary mechanisms responsible for the observed deformation behavior; moreover, the strain rate was found to increase with decreasing grain size. These observations were confirmed in subsequent simulations in the temperature range of 300–500 K and for grain sizes of up to 12 nm [92,93] and later 20 nm [129] and it was suggested that GB sliding takes place through atom shuffling and “stress-induced” (i.e., athermal) GB diffusion [93,129]. Similar to the work of Schiotz et al., these simulations also revealed the nucleation of Shockley partials above a certain minimum grain size, d_m , which was shown to depend on the stacking-fault energy ($d_m \sim 8$ nm for Cu and ~ 12 nm for Ni; [93]).

In spite of these rather similar observations, the two groups have offered qualitatively different interpretations. Schiotz et al. plotted their yield and flow stresses

against $d^{-1/2}$ (see Fig. 15), supposedly confirming the proposed form for the inverse Hall–Petch effect [8], however without offering a physical explanation of the $\sigma_Y \sim d^{1/2}$ dependence. Also, while observing extensive partial-dislocation nucleation from the GBs, they showed that these dislocations were responsible for only about 1/3 of the total plastic strain, leading them to conclude that GB sliding is the dominant deformation mechanism, rather than dislocation slip. Unfortunately, however, the accommodation process required for GB sliding to proceed was not addressed.

By contrast, Swygenhoven et al. [93,129] plotted their strain rates against d^{-1} (see Fig. 16(a); i.e., assuming that $\sigma_Y \sim d$ rather than $\sigma_Y \sim d^{1/2}$). Whereas the strain rates for the three smallest grain sizes were shown to be associated with GB sliding as the sole deformation mechanism, the deformation behavior for the two largest grain sizes involved both GB sliding and dislocation processes. The GB sliding-dominated behavior was rationalized on the basis of a simple model which, like Schiotz et al., assumes that the entire macroscopic deformation arises from GB sliding. Assuming further that deformation occurs by a viscous type flow of the grains, with a viscosity governed by stress-driven, thermally activated GB sliding, a simple GB-area to GB-volume argument was then shown to lead to a d^{-1} dependence of the strain rate, according to [93]:

$$\dot{\epsilon}(\sim 1/\sigma_Y) = \frac{\dot{d}_0}{d} e^{-(U/kT)} \sinh\left(\frac{\sigma v}{kT}\right), \quad (2)$$

where \dot{d}_0 is a characteristic elongation rate of a grain of size d [129], v is the activation volume and U the activation energy for GB sliding. We note that this expression, and the manner in which it was derived, differs fundamentally from (i) the expression for dislocation-induced GB sliding as a mechanism controlling the strain rate in superplastic deformation (yielding the usual $\dot{\epsilon} \sim d^{-2}$ dependence; [130]), and (ii) from Coble's expression

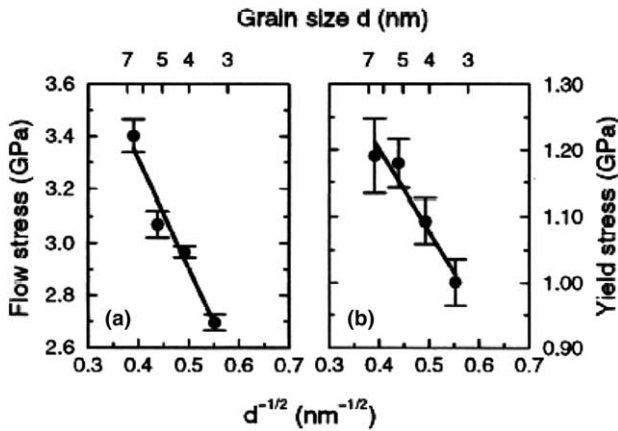


Fig. 15. Grain-size dependence of yield stress (a) and flow stress (b) extracted from room-temperature MD simulations of Schiotz et al. [23].

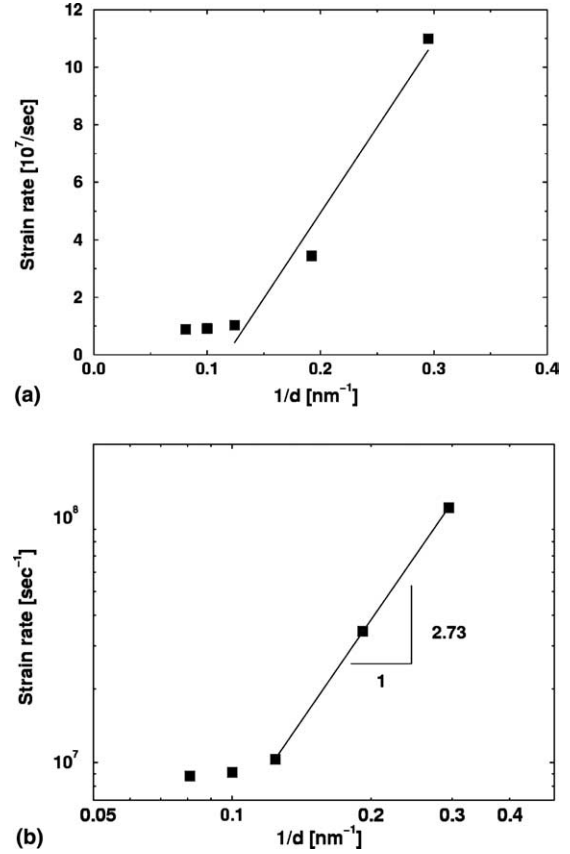


Fig. 16. Grain-size dependence of strain rates extracted from room-temperature MD simulations of Swygenhoven et al. [93] of a nanocrystalline-Ni model system containing only high-angle GBs. The grain sizes ranged between 3.4 and 12 nm. Whereas for the two largest grain sizes the deformation is governed by a dislocation process, the deformation behavior for the three smallest grain sizes is due to GB processes [93]. (a) Strain rates plotted against $1/d$, as in the original work [93]; the straight line suggests that Eq. (2) is obeyed. (b) Doubly logarithmic plot of the same data, revealing a perfect fit of the data points for the three smallest grain sizes to the Coble-creep equation (see Eq. (3) below).

[38] for GB diffusion accommodated GB sliding (see Eq. (3) below).

The key question about these simulations is this: if (i) GB sliding is, indeed, the dominant deformation mechanism and if, indeed, (ii) dislocation processes play no role in the deformation – at least for the smallest grain sizes – and if (iii) microcracking does not occur, then what choices are left for the (rate-limiting) accommodation mechanism? The suggestion that “stress-assisted GB diffusion” may accompany the observed GB sliding [129] might offer a clue. If this were the case, then the accommodation mechanism should be the same as in Coble creep, the only difference being the absence of an activation energy for this athermal process; the Coble-creep formula should then apply. To test this hypothesis, in Fig. 16(b) the data from Fig. 16(a) [93] are replotted, however, as a doubly logarithmic plot. Remarkably, the data points for the three smallest grain

sizes fall on a straight line with a slope of 2.73. As expected for the Coble-creep mechanism [38], the magnitude of this slope confirms that GB diffusion, albeit likely of athermal origin, accommodated by GB sliding or, conversely, GB sliding accommodated by stress-induced atom reshuffling that resembles GB diffusion, is responsible for the simulated deformation behavior (see also Section 4.2).

As discussed in detail in Section 4.4, the above analysis illustrates a response of the system in a temperature/strain-rate/stress regime where the underlying thermal-equilibrium, steady-state deformation process cannot be probed due to the far too short MD time window at room temperature. However, it is interesting to observe that in the absence of any of the usual accommodation processes, the simulated system [123] nevertheless finds a deformation mode that can at least be rationalized.

4.2. Simulation of grain-boundary diffusion creep

Apart from GB sliding, it has been proposed that even at relatively modest temperatures, nanocrystalline fcc metals with the smallest grain size may deform by the mechanism of Coble creep and that this might explain the observations of inverse Hall–Petch behavior for $d < d_c$ [8,9]. To test this suggestion, Yamakov et al. [131] performed MD simulations of fully 3d nanocrystalline Pd microstructures with a grain size of up to 15.2 nm. To render the process observable on an MD time scale and at relatively low stresses (of 100–400 MPa, i.e., well below the dislocation-nucleation threshold; see Section 3.1), the simulations were performed at elevated temperatures ranging from 900 to 1300 K, i.e., 0.6 – $0.9T_m$ for the Pd (EAM) potential [54,55]. As in the earlier simulations of GB diffusion creep in nanocrystalline Si [37], in order to suppress grain growth and thus enable steady-state diffusion creep to take place, model microstructures were tailored to have a uniform grain size and shape. The random grain orientations chosen in this study ensured that all the GBs in the system were high-energy boundaries, whose structure and self-diffusion behavior had been studied previously [50,54] using the same interatomic potential for Pd [55].

According to Fig. 17, following an elastic regime the simulations reveal the onset of steady-state creep, characterized by constant strain rates. These rates were found to increase linearly with the applied stress, σ , for the entire range of grain sizes and temperatures investigated [131]. Moreover, by following the displacements of the centers of mass of individual grains, as in the earlier nanocrystalline Si deformation simulations [37], the deformation was verified to be homogeneous, i.e., the deformation of each grain mirrors the overall deformation.

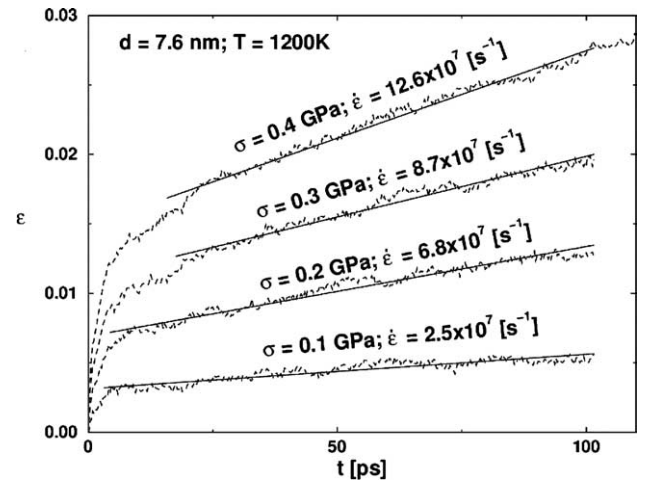


Fig. 17. Total (elastic + plastic) strain vs. simulation time of a tailored, 3d periodic nanocrystalline Pd microstructure consisting of 16 grains of identical shape and grain size (of 7.6 nm) arranged on a bcc lattice at 1200 K under different tensile stresses [131].

The activation energy represents an important fingerprint of the underlying deformation mechanism. The Arrhenius plot in Fig. 18 for the strain rates extracted from the simulations (Fig. 17) yields an activation energy of 0.61 ± 0.1 eV. This value is in remarkable agreement with the universal high-temperature activation energy of 0.60 ± 0.05 eV determined earlier [54] for high-energy *bicrystalline* GBs in Pd in the absence of stress and of any of the microstructural constraints present in the polycrystal (see Fig. 7 and Section 2.3). This comparison reveals that, indeed, GB diffusion is the deformation rate-limiting process.

The grain-size dependence of the strain rate represents another important characteristic of the deformation mechanism. The observed linear relation between $\dot{\epsilon}$ and σ [131] suggests that, for a given grain size and temperature, the strain rates obtained for different stresses (Fig. 17) should – within the error bars – collapse

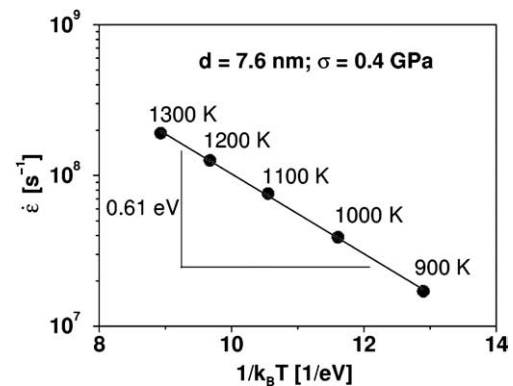


Fig. 18. Arrhenius plot for the creep rate in the same 16-grain simulation model used in Fig. 17 [131]. The error bars are negligible on this scale (of the order of the symbol size) and are not given.

into a single point, $\dot{\epsilon}/\sigma$. The log–log plot of $\dot{\epsilon}/\sigma$ vs. the grain size in Fig. 19 collects all the data points thus obtained at 1200 K. In this representation the strain rates, indeed, fall on a universal curve, showing a d^{-3} dependence for the larger grain sizes and close to a d^{-2} dependence for the smaller ones.

Taken together, the observations of (i) the linearity between $\dot{\epsilon}$ and σ , (ii) the homogeneity of the deformation, (iii) the correct activation energy (namely that for GB diffusion), and (iv) the d^{-3} dependence found for the larger grain sizes demonstrate that the simulation results for the larger grain sizes are consistent with the well-known Coble-creep formula [38],

$$\dot{\epsilon} = A \frac{\sigma \Omega_D}{k_B T} \frac{\delta_D D_{GB}}{d^3}. \quad (3)$$

Here, $\delta_D D_{GB}$ is the diffusion flux in the GBs with diffusion constant D_{GB} , grain-boundary width δ_D and activation volume Ω_D . $\sigma \Omega_D$ is the work performed by the stress during an elementary diffusion jump in the GB; $k_B T$ is the thermodynamic temperature and A is a geometric constant which depends on the grain shape. To test whether the underlying mechanism is indeed that assumed by Coble, the authors followed the diffusion of individual GB atoms, verifying that, indeed, they diffused from the grain equators to the poles [131].

By contrast with Eq. (3), for the two smallest values of d deviations from the d^{-3} dependence are clearly visible in Fig. 19. This reduced grain-size dependence for the smallest values of d was shown to follow naturally from Coble's derivation under the assumption that the GB width can no longer be neglected relative to d . In

this limit, Coble creep and Nabarro–Herring creep become identical processes, with a grain-size exponent of -2 (see Fig. 19) [131].

4.3. Geometrically necessary coupling between grain-boundary diffusion creep and grain-boundary sliding

From the deformation of coarse-grained materials under conditions where dislocation processes are unimportant and microcracking does not occur, it is well-known that, just as GB sliding must be accommodated by GB diffusion [132], GB diffusion creep in turn requires GB sliding (known as Lifshitz sliding [133,134]) as an accommodation mechanism. The interplay between the two mechanisms therefore represents two different aspects of the same deformation process.

Throughout their simulations, Yamakov et al. [131] verified that no dislocations were nucleated from the GBs (see also Section 3) and that no microcracking occurred. Under these conditions, the GB diffusion creep should be accommodated by Lifshitz sliding [133,134]. Experimentally GB sliding can be observed directly by scratching marker lines across the GBs [135]. Since in MD simulations the atoms are already labeled, this idea was implemented [131] by “painting” straight lines of atoms across the surface of the unstrained system. These simulations revealed that after $\sim 4\%$ elongation in the tensile direction, the marker lines had, indeed, undergone shifts across all the GBs. A detailed analysis of the magnitudes of these shifts showed them to be in complete agreement with the geometrically necessary “Lifshitz sliding” required to accommodate the GB diffusion creep [133,136]. We note that this type of GB sliding is distinct from Rachinger sliding [134,137] which occurs when, during *large-strain* deformation, entire grains move through the polycrystalline matrix. Rachinger sliding is therefore an *inhomogeneous* deformation process and involves topological discontinuities, such as neighbor switching [138].

4.4. Discussion

The results of the significant number of simulations of inverse Hall–Petch behavior reviewed above strongly suggest that in the absence of grain growth, the nanocrystalline microstructures considered in these simulations deform via the well-known Coble-creep mechanism. The inverse Hall–Petch effect therefore appears to be merely a manifestation of GB diffusion creep, with the characteristic d^{-3} decrease of the creep rate with decreasing grain size. The apparently contradictory suggestions that GB sliding, on one hand, and GB diffusion creep, on the other, are responsible for the inverse Hall–Petch effect can thus be reconciled as originating from one and the same deformation mechanism.

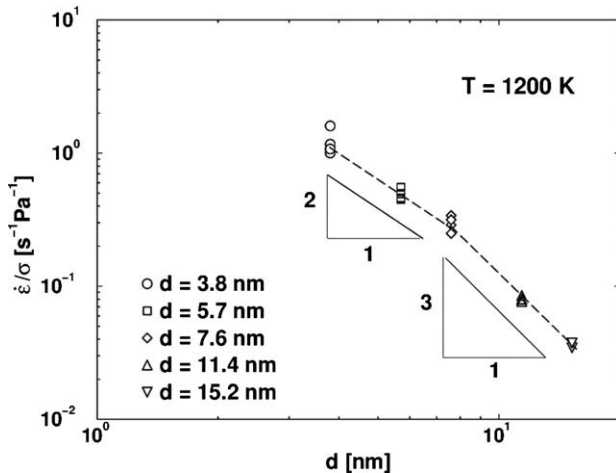


Fig. 19. Scaling plot of $\dot{\epsilon}/\sigma$ vs. grain size, d , showing that all the data points obtained for different stresses at 1200 K collapse onto a single curve, and indicating that the strain rate increases linearly with stress (see Eq. (1)). The dashed curve is merely a guide to the eye. The error bars of these independent simulations are equal to the scattering of the data points around this curve for each of the given grain sizes and are not given for clarity. The increased scattering with decreasing grain size is due to the greater equilibrium fluctuations in the smaller systems [131].

However, given that GB diffusion is a thermally activated process, one cannot hope to prove directly by MD simulation that the observation of thermal equilibrium Coble creep [131] can be extrapolated to room temperature where most deformation experiments are performed. Whereas the observation window accessible to MD simulations is limited to typically less than about 10^{-8} s, the experimental time window is typically ten orders of magnitude longer. In order for MD simulations to nevertheless capture the *equilibrium* steady-state response of the material at lower temperatures *and* under experimental conditions, much longer simulation times than those presently possible would therefore be required. Since this is not an option, the challenge consists in capturing and elucidating the rate-limiting experimental processes, however within the short MD time window, while avoiding probing some poorly defined, “MD only” deformation rate-dependent transient response of the material.

To analyze quantitatively whether in Pd, at least experimentally, Coble creep can be expected to facilitate the deformation even at room temperature and at a more typical stress level of $\sigma = 0.1$ GPa, Eq. (3) can be extrapolated to determine the predicted strain rate based on the simulation results described in Sections 4.2 and 4.3 [39]. Starting from the simulated strain rate of $\dot{\epsilon}(900 \text{ K}, 0.4 \text{ GPa}) = 1.7 \times 10^7 \text{ s}^{-1}$ obtained for a grain size of 7.6 nm at 900 K for $\sigma = 0.4$ GPa (see Fig. 18), with the activation energy of 0.61 eV one finds:

$$\begin{aligned} \dot{\epsilon}(300 \text{ K}, 0.1 \text{ GPa}) &= 1.1 \times 10^{-7} \dot{\epsilon}(900 \text{ K}, 0.4 \text{ GPa}) \\ &= 1.87 \text{ s}^{-1}, \end{aligned} \quad (4)$$

i.e., a strain rate entirely within the experimental range. Under these conditions, particularly in the absence of dislocations, GB sliding can, indeed, be accommodated by GB diffusion. This is remarkable because for Pd, with a melting point for the potential used here of about 1500 K, room temperature represents a homologous temperature of only ~ 0.15 .

Since experimental strain rates are usually even lower than the limit in Eq. (4), it seems entirely plausible that, as predicted over a decade ago by Gleiter and his co-workers [3,8,9], even at room temperature most nanocrystalline fcc metals can, indeed, deform via the Coble-creep mechanism. Unfortunately, however, this assertion cannot be proven directly by MD simulation since an MD time window of ~ 1 s would be required to observe thermally activated GB diffusion. However, as illustrated in Fig. 16(b), even the room-temperature MD simulations are consistent with the Coble-creep mechanism [93,128], in spite of the fact that the time window in these simulations was far too short to capture the equilibrium GB diffusion process. It is interesting to observe that in the absence of any of the usual accommodation processes, including *thermally activated* GB

diffusion, microcracking and dislocation processes, and under simulation conditions corresponding to no experimentally realizable situation, the simulated system [93,128] finds a deformation mode that can at least be rationalized. These observations suggest that Coble creep, i.e., GB diffusion-accommodated GB sliding, represents a very robust mechanical response of a nanocrystalline material, even at low temperatures. The reasons for this probably lie in the fact that GB diffusion, or even athermal stress-induced shuffling of GB atoms, represents a very powerful stress-relaxation mechanism.

The study of Yamakov et al. [131] demonstrates that under carefully chosen simulation conditions, the well-known time-scale and high-stress limitations inherent to MD simulations can be overcome to enable probing the intrinsic equilibrium steady-state response of a nanocrystalline microstructure to external loading. Although limited to elevated temperatures, under these thermodynamically and kinetically well-defined conditions Yamakov et al. were able to elucidate the role of GB diffusion as an accommodation mechanism for GB sliding, and vice versa. However, this study also demonstrates the considerable difficulties of such simulations in capturing the equilibrium steady-state response of the material at lower temperatures, the challenge being to avoid probing some poorly defined, deformation-rate dependent transient response of the material which cannot easily be related to the deformation conditions present in experiments.

4.5. Comparison with experiments

Experimental studies on the deformation mechanisms at grain sizes of the order of a few nanometers have attracted a great deal of attention over the last few decades. Despite the numerous observations published so far (see, e.g., Fig. 20), the situation remains controversial, primarily due to the experimental difficulties associ-

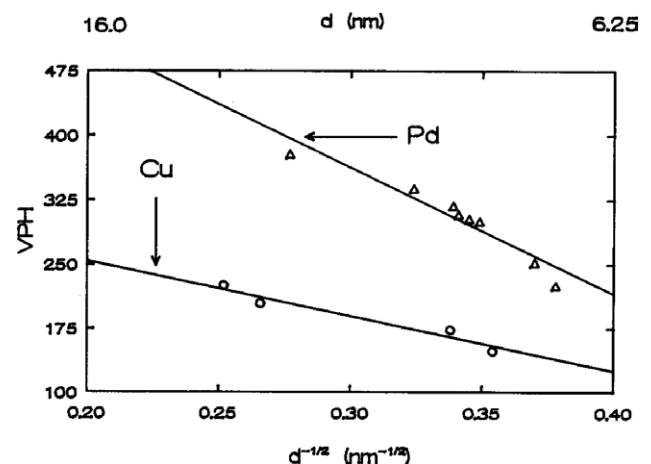


Fig. 20. Hardness of nanocrystalline Cu and Pd plotted against $d^{-1/2}$ [8].

ated with these studies. The preparation of bulk nanocrystalline specimens that are free from microstructural defects (e.g. voids) and free of contaminations is still a challenge. Moreover, the measurements as well as the microstructural studies of the deformed state have encountered several difficulties. The papers published in this field have been reviewed recently by Weertman [139] and Milligan [140].

Extensive plastic deformation (in some cases beyond 100%) of nanocrystalline metals [126,141], alloys [4,126] as well as ceramics [3] was reported. The explanations proposed for these observations are based on the assumption that the large fraction of atoms located at the GBs was responsible for plastic deformation and that GB diffusion dominates the deformation process. Since then, the original models based on Coble creep [8,11] have been refined to account for dislocation activity, GB and lattice diffusion [142], and triple junction diffusion [143]. More generally, Mukherjee [36] has recently pointed out that the deformation of nanocrystalline materials follows traditional constitutive laws for plasticity, but with important differences in the level of stress, strain-hardening rate, and temperature dependence.

This view seems to agree with recent deformation studies on nanocrystalline Fe. Mara et al. [144] produced 15–20 nm size alpha-iron grains by controlled crystallization of Fe-based metallic glass. They observed negligible (<1%) ductility and very high flow stresses (of 1200 MPa) at a strain rate of 10^{-4} s^{-1} . However, when tested at the same strain rate but at 725 °C, where the grains have grown to $d \sim 100 \text{ nm}$, the ductility increased to 65% and the flow stress dropped to about 125 MPa. This clear transition is very likely associated with the absence of dislocation-mediated plasticity at 600 °C (for $d \sim 15 \text{ nm}$) and its presence at 725 °C (for $d \sim 100 \text{ nm}$). The same conclusion is suggested by a recent detailed deformation study on micro- and nanocrystalline Pd [109], with grain sizes of $d > 100 \text{ nm}$ and $d > 11 \text{ nm}$, respectively. After 68% deformation by rolling, TEM micrographs of both kinds of specimens revealed equiaxed grains in the nanocrystalline and elongated ones in the microcrystalline specimen. This change in grain shape was accompanied by a different development of the texture of the two specimens, both of which were initially free of texture [109]. As further discussed in Section 5.4.1 (cf. Fig. 29), the nanocrystalline material remained texture free whereas the microcrystalline samples developed the rolling texture typical for fcc metals [109]. The lack of crystallographic textures and the equiaxed grain shape in the strongly deformed nanocrystalline material are consistent with findings for superplastic deformation, indicating that GB sliding is active – in agreement with observations from MD simulations – and that intragranular deformation by dislocation activity is less dominant than in coarse-grained fcc metals.

Remarkably, some of the micrographs of the nanocrystalline material show neighboring segments of GBs to be aligned in parallel, the signature of macroscopic shear-band formation. This suggests that the deformation, at least in the later stages, is adequately described by a model based on GB sliding over coplanar arrays of GBs. This result agrees with earlier experiments [145,146] and the MD simulations [30,31].

In creep tests, both kinds of Pd samples exhibited a slow contraction in the absence of an applied load; this is presumably due to sintering, and evidences noticeable atomic mobility at room temperature. The creep experiments (performed at 313 K) were carried out by using samples with the same grain size of 10 nm in two different strain-rate regimes (of 10^{-10} and $6 \times 10^{-2} \text{ s}^{-1}$). For the creep tests at the rate of 10^{-10} s^{-1} , the rate-controlling deformation process was identified by comparing the experimental data with the creep rates predicted by Nabarro–Herring or Coble creep, fitting the diffusion coefficients for volume and GB diffusion, D_V and D_{GB} , respectively to the experimental data. The results obtained were $D_V = 10^{-26} \text{ m}^2/\text{s}$, $D_{GB} = 5 \times 10^{-27} \text{ m}^2/\text{s}$. These numbers have to be compared to the values obtained by extrapolating the appropriate diffusion data from the literature [147] to $T = 313 \text{ K}$. In this way one obtains $D_V = 10^{-49} \text{ m}^2/\text{s}$ and $D_{GB} = 10^{-28} \text{ m}^2/\text{s}$. The discrepancy between the experimental value for D_V and that extrapolated from the literature rules out Nabarro–Herring creep as the dominant creep mechanism. By contrast, and in view of the considerable uncertainty in extrapolating diffusion data to room temperature, the value of D_{GB} obtained based on the assumption of Coble creep as the dominant mechanism is in quantitative agreement with the D_{GB} data in the literature. This supports the view that the deformation of nanocrystalline Pd in the limit of small stresses is mediated by GB diffusion, in qualitative agreement with the MD simulations (see Fig. 18). For the fast deformation, X-ray diffraction measurements [147] revealed an increase in stacking-fault density during the initial stages of deformation, an indication of dislocation activity within the grains. However, the absence of a rolling texture and the equiaxed grain shape after large deformation are more compatible with mechanisms based on GB sliding, similar to superplastic deformation. The observation of mesoscopic glide planes formed by the local alignment of adjacent GBs suggests that it is this process that results in the formation of co-planar arrays of GBs, leading to a process of cooperative GB sliding when observed at the mesoscopic scale [148,149].

Although the experimental studies mentioned so far seem to demonstrate convincingly the plastic deformation of nanocrystalline materials at ambient temperature, the low-temperature ductility of these materials is still a matter of controversy [140]. For example, Sanders et al. [150] could not detect any ductility in nanocrystalline

Cu if the grain size was less than 49 nm. This lack of ductility may be associated with porosities and/or contaminants picked up during the consolidation steps. This result seems to disagree with other measurements on the same material [108,141]. Even at grain sizes between 25 and 30 nm, a plastic strain of about 2% was noticed. However, careful material characterization revealed a fraction of coarser grains which may or may not be the cause for the plasticity. The very large ductility associated with cold rolling of Cu at room temperature [141] may not be associated with true nanocrystallinity. The nanosize “grains” are very likely dislocation cells separated by low-angle cell boundaries. The remarkably low stresses encountered in this investigation also attest to the possibility that the material is not “nanocrystalline” in the true sense of the word. Carsley et al. [151] conducted a study of ball-milled nanostructured Fe alloys. An unusual deformation mechanism was observed in all tests: the specimens exhibited perfectly plastic behavior and deformed by shear banding. However the shear bands were not on the planes of maximum shear or zero extension, and there was a substantial tension–compression asymmetry in the yield strength. This led the investigators to propose that flow is controlled by hydrostatic pressure, similar to glassy metals and polymers [151–153]. Similarly, nanocrystalline Al alloys [107] exhibited a tension–compression asymmetry and perfect plasticity, but no shear instability. The same behavior has been reported for ultrafine-grained aluminum alloys [154] and a titanium alloy [155]. Based on these results, it seems plausible that ultrafine-grained metals may generally be stronger in compression than in tension, and that bcc metals may generally be subject to deformation instabilities while fcc metals can deform homogeneously.

In summary, the existing body of experimental evidence seems to be divided into the following two groups. One group comparing pure metals, metallic alloys and ceramics revealed clear evidence for plastic deformation of nanocrystalline materials. Diffusional processes including GB shear seem to be predominant. These findings agree well with the MD results. This conclusion disagrees, however, with several other studies, sometimes on the same material (e.g. Cu). One cause for this discrepancy may be that materials with the same chemical composition but with different microstructures were investigated. The work by Legros et al. [108] has demonstrated the importance of the microstructure in terms of the grain-size distribution. It seems conceivable that in the different studies variations of the grain-size distributions were not detected by the characterization methods applied. Hence, in view of the obvious discrepancies between the two groups of experimental results, a critical study elucidating the reasons for these discrepancies seems to be crucially needed. One of the obvious model systems for such a study may be nanocrystalline Cu,

which has been reported to exhibit virtually no ductility [150] and has also been deformed without fracture by more than 100% [141]. The open question that remains, is: What are the critical parameters that distinguish the two types of nanocrystalline Cu?

4.6. Critical issues and outstanding questions

MD simulation has clearly revealed that GB sliding does take place in very small-grained nanocrystalline materials. The important question is: What is the relevant accommodation process? If stress-assisted GB diffusion accompanies the GB sliding, then the accommodation mechanism should be similar to Coble creep, albeit with an athermal activation energy. The replotted data in Fig. 16(b) strongly supports this conjecture, i.e., GB sliding is accommodated by stress-induced atom shuffling that resembles GB diffusion. The fully 3d MD simulations of Coble creep at elevated temperatures by Yamakov et al. [131] for nanocrystalline Pd yielded an activation energy for creep remarkably equal to the activation energy for diffusion in high-energy bicrystalline GBs. Since in the bicrystal simulations, no stress was applied and no microstructural constraints, (such as triple-points, etc.) were present, this correlation strongly suggests that GB diffusion is the rate-controlling process in such deformation. This points to the essential physical fact that GB diffusion (as in Coble creep) or athermal stress-induced shuffling of GB atoms (as in GB sliding), represents a very effective stress-relaxation mechanism.

Several experimental results on large-strain deformation of nanocrystalline metals demonstrate a lack of texture formation and the retention of equiaxed grains. These observations are compatible with the operation of a GB-sliding related superplasticity-type mechanism, revealing that the mesoscopic-level glide planes formed by the local alignment of adjacent GBs results in the formation of coplanar arrays of GBs. This should lead to a process of cooperative GB sliding that has been convincingly demonstrated in microcrystalline materials [148,149] but not in nanocrystalline materials.

In general, quite a few nanocrystalline pure metals and metallic alloys reveal clear evidence of plastic deformation in which diffusional processes, including GB sliding, dominate. These results agree well with the predictions from the MD simulations. However, there is now also a significant body of literature on nanocrystalline metals where such ambient-temperature ductility is not evident. As discussed in Section 4.5, some investigators have suggested that this difference may be due to differences in grain-size distribution in the experimental material. One major cause for this discrepancy could also be that, although different investigators are referring to nominally the same metal (or material), their actual chemistries may not be the same due to the

differences in processing routes. It is interesting to note that nanocrystalline metals produced by consolidation of either ball-milled powders or powders produced by inert-gas condensation, have often revealed shear banding during deformation, similar to glassy metals and polymers. Such a deformation behavior, typical of a non-crystalline matrix, suggests that perhaps exceptionally small and finely dispersed impurities (oxides, carbides, etc.) in the microstructure, picked up during the processing steps, may be responsible for this behavior. In this context, there is a need for carefully documented investigations to remove these glaring discrepancies related to ductility in nanocrystalline microstructures, e.g., in Cu, as described in Section 4.5.

5. Crossover from ‘normal’ to ‘inverse’ Hall–Petch behavior

Facilitated by rapid increases in computational power, two recent simulation studies on fully 3d microstructures [29,156] have been able to capture the full range of grain sizes over which the crossover from a dislocation process (see Section 3) to a GB process (see Section 4) takes place, and thus to elucidate the nature of the ‘strongest grain size’, d_c , in nanocrystalline fcc metals. In the first of these studies, Yamakov et al. [29] considered nanocrystalline Al microstructures consisting of four grains in a periodically repeated simulation cell. This simple setup enabled exploration of a range of grain sizes from 7 to 32 nm, i.e., both above and below d_c for Al, and hence allowed the transition from GB-dominated processes (for $d < d_c$) to dislocation-dominated processes (for $d > d_c$) to be directly probed (see Section 5.2). Most importantly, these simulations demonstrated for the first time directly the coupling between the crossover in the deformation mechanism and the mechanical behavior. In addition to yielding a value of $d_c \sim 18$ nm for Al, these simulations demonstrated unambiguously that the crossover in the mechanical behavior is, indeed, due to a transition in the dominant deformation process.

In the second study, Schiotz and Jacobsen [156] determined the flow stress of nanocrystalline Cu with a grain size ranging between 5 and 50 nm. These simulations also revealed the expected crossover in the flow stress, from Hall–Petch to inverse Hall–Petch behavior, at a value of $d_c \sim 14$ nm for Cu. As in the study of Yamakov et al., this crossover in the mechanical behavior was accompanied by a change in the underlying mechanism, from dislocation-mediated plasticity to GB sliding.

In the following, we summarize some of the key insights gained from these studies.

5.1. Grain boundaries as dislocation sources

In the simulations by Yamakov et al. [29] four grains of identical size and a rhombic-dodecahedral shape (the

shape of the fcc Wigner–Seitz cell) were arranged on a 3d periodic fcc lattice. The 24 GBs in the simulation cell thus meet at 32 triple lines at 120° angles, i.e., close to the equilibrium Herring angles, ensuring a high degree of stability against grain growth. By selecting random grain orientations and applying a Monte–Carlo procedure to avoid low-angle and vicinal (i.e., dislocation) boundaries as well as “special” high-angle misorientations, they ensured that, as in their columnar model (see Section 3), all the GBs in the system were general, high-energy GBs with a highly disordered atomic structure (see Section 3.1). This simulation geometry ensures a rather uniform stress distribution across the microstructure [157,158]. In spite of the small number of grains, elevated-temperature simulations of GB-diffusion creep in nanocrystalline Si [37] and Pd model systems with the same geometry (see also [131,159]) quantitatively reproduced the Coble-creep formula for the strain rate (see Eq. (3)).

The first important result of Yamakov et al. [29] was the observation (see Fig. 21) that the GBs in their fully 3d microstructure, indeed, nucleate perfect dislocations, as suggested by Li [125] 40 years ago. As in their columnar model geometry [25], these dislocations were found to be $1/2[110]$ dislocations dissociated into two $1/6[112]$ Shockley partials connected by a stacking fault, i.e., the type of extended dislocations commonly seen in fcc metals [90]. In the formations labeled 1 in Fig. 21(a) and (b), these dislocations are seen as red loops representing the stacking-fault atoms in an hcp environment, delineated by two thin blue lines of atoms representing the dislocation lines of the two partials. The simulations revealed that the mechanism of nucleation of these extended dislocations involves the successive emission of both the leading and trailing Shockley partials from the GB (see also [25]). As in the columnar simulations, the width of the stacking-fault region, i.e., the splitting distance, r , of the extended dislocation, depends on the resolved shear stress and the stacking-fault energy (SFE) as expressed by Eq. (1) (see Section 3.2). Once nucleated, these dislocations grow and extend into the grain interiors.

It is well known that dislocation loops in coarse-grained materials are formed by Frank–Read sources. The difference here is that the range of grain sizes (of 7–32 nm; see Fig. 21) is too small for complete loops to develop. As the loop radius is inversely proportional to the resolved shear stress, it cannot be made smaller than the grain size for any reasonable value of the stress; the dislocation is thus forced to terminate at the GBs. Hence, although Fig. 21(a) and (b) reveal the onset of the dislocation-slip mechanism, the GBs still strongly affect the process by modifying the dislocation mobility. In particular, it seems likely that the dislocation mobility is decreased due to its termination on GBs, suggesting a GB-induced mechanism for hardening with decreasing

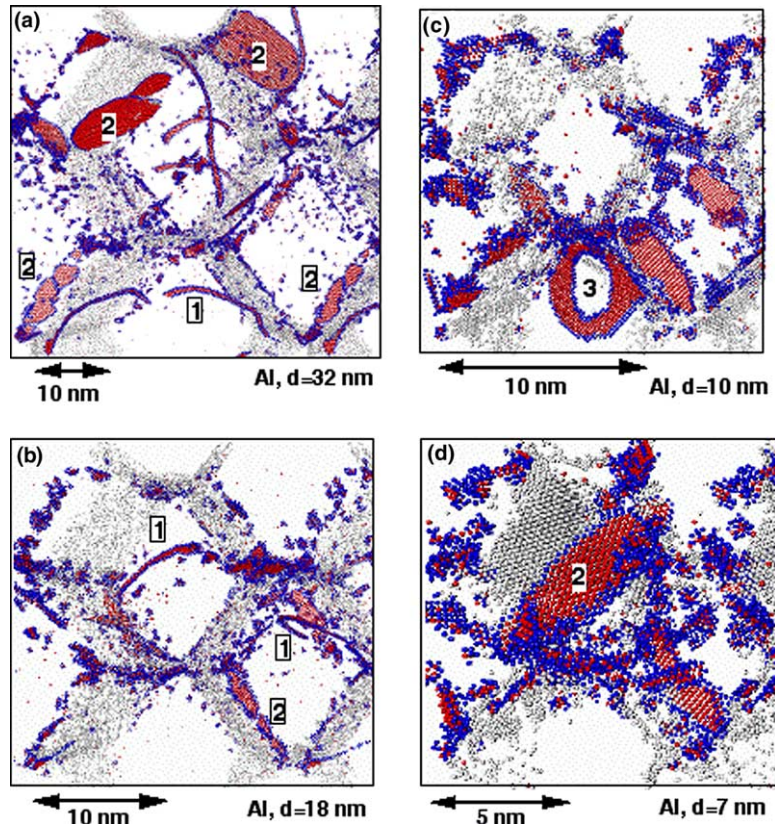


Fig. 21. Snapshots of the four-grain, fully 3d Al microstructure at about 1.5% plastic strain for four different grain sizes: (a) $d = 32$ nm; (b) $d = 18$ nm; (c) $d = 10$ nm and (d) $d = 7$ nm. Common-neighbor analysis was used to identify atoms as being either in a local hcp (red atoms) or fcc environment (not shown). The GBs are seen as walls of gray atoms (representing “disordered” atoms, i.e., atoms neither in a local fcc nor hcp environment). To better visualize the grain interiors, only parts of the GBs are shown. The blue atoms are “highly disordered” atoms, defined as (i) atoms with more than half of their neighbors within the cut-off radius of the potential being disordered or (ii) atoms interacting with at least two hcp coordinated atoms. Three distinct types of dislocation configurations are labeled as (1), indicating a complete, extended $1/2[1\ 1\ 0]$ dislocation; (2), indicating a stacking-fault plane produced by a single Shockley-partial dislocation and (3), split stacking-fault plane [29] (For interpretation of the references to color in this figure legend, the reader is referred to the Web version of this article).

grain size. This mechanism could supplement the conventional dislocation pile-up mechanism in which the GBs act as barriers impeding the free movements of the dislocations.

The mechanism by which dislocations are nucleated is revealed in the atomic-resolution snapshot shown in Fig. 22, representing a cross-section of the microstructure through the nucleation point of a dislocation perpendicular to the dislocation line. In this case, the nucleation takes place at a ledge at one of the eight-fold point junctions in the system (appearing as a quadruple junction in the cross-section). The moment at which the trailing partial of the dislocation is nucleated is captured to the right of this junction; this event completes the process of the nucleation of this perfect, extended dislocation. On the opposite side of the junction in Fig. 22 one can see the initial stage of nucleation of another partial dislocation; shortly thereafter this resulted in the emission of another dislocation loop. These observations support the idea, put forward by Li [125] 40 years ago, that GBs can nucleate dislocations from ledges. In addition to the process of dis-

location nucleation, the small 3d island of fcc atoms in Fig. 22 reveals the early stage of recrystallization starting at the junction.

A comparison of these observations for a fully 3d microstructure with those obtained for a columnar simulation geometry [25] reveals that, not surprisingly, the main difference lies in the fact that in the 3d microstructure, the dislocation lines are no longer constrained to being straight lines. This allows the development of dislocation loops, the curvature of which introduces a grain-size effect into the nucleation stress. By relating the size of the dislocation loops nucleated from the GBs to the grain size, Cheng et al. [107] recently suggested that the nucleation stress should be inversely proportional to the grain size, $\sigma_n \sim 1/d$. As a consequence, when the grains become larger (say of μm size), the mechanism changes to the one considered by Li [125] involving the nucleation of dislocations from GB ledges and their propagation through the forest dislocations commonly present in coarse-grained materials. This mechanism gives a Hall–Petch type of nucleation stress, $\sigma_n = \sigma_0 + k/\sqrt{d}$, where σ_0 is the single-crystal yield stress

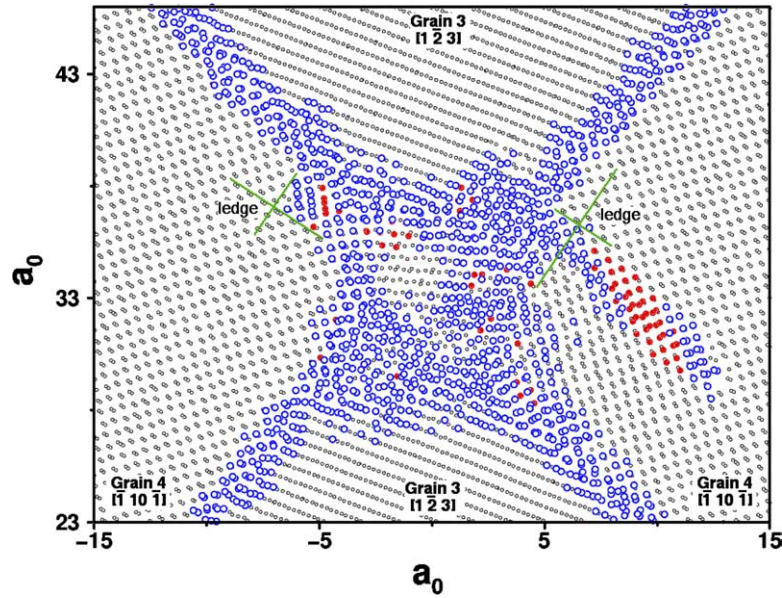


Fig. 22. Atomic-resolution snapshot of a cross-section taken through the nucleation point of a dislocation perpendicular to the dislocation line. As in Fig. 21, the stacking-fault atoms are shown in red, disordered atoms in blue and the remaining ones, in perfect fcc-crystal surroundings, are shown as black open circles. In addition to the process of dislocation nucleation, the small 3d island of fcc atoms reveals the onset of recrystallization (For interpretation of the references to color in this figure legend, the reader is referred to the Web version of this article).

and k is a constant that depends on the strength of the GB. Combining the two mechanisms one gets:

$$\sigma_n = \sigma_0 + \kappa/\sqrt{d} \quad \text{for coarse} \\ \text{— grained metals [125],} \quad (5a)$$

$$\sigma_n \sim 1/d \quad \text{for nanocrystalline metals [27,107].} \quad (5b)$$

A similar Hall–Petch form of Eq. (5a) has recently been discussed also by Bata and Pereloma [160]. The increase of σ_n with decreasing grain size would imply a decrease in the dislocation activity in smaller grains. This decrease is clearly seen in Fig. 21(a)–(c). The absence of such a decrease in the columnar-model simulations [25] supports the role of the dislocation-line curvature in the nucleation process. Also, for the same grain size and interatomic potential the 3d model microstructures exhibited a slightly lower threshold stress for dislocation nucleation from the GBs (of ~ 1.9 GPa; [29]) than the columnar systems (of ~ 2.3 GPa). This difference is probably due to (i) the fact that the dislocations are no longer restricted to being straight lines (see Fig. 21), and (ii) the presence of a complete set of 12 slip systems (compared to only six in the columnar microstructures).

We finally mention that, in addition to the nucleation mechanism involving the successive emission of two complementary partial dislocations, Fig. 21(c) reveals a second mechanism for producing a perfect dislocation. This mechanism starts by the nucleation of a single partial from the GB, leaving an intrinsic stacking fault behind (formation 3 in Fig. 21(c)). At some point, instead of nucleating a follow-up second partial, the

stacking-fault plane breaks from inside, producing a loop of another partial dislocation which restores the fcc lattice (see formation 3). The result is a perfect dislocation loop in close vicinity to the GB.

Such an event has also been observed in atomistic simulations of a Frank–Read source using the same EAM potential for Al [161]. The authors refer to this effect as “anomalous dislocation multiplication in fcc metals” [161]. A careful estimate of the resolved shear stress required to split the stacking fault gave a value of 0.93 ± 0.05 GPa. This value is consistent with a previous estimate of 1 GPa for the resolved shear stress on the (1 1 1) planes using the same potential [25]. While the size of the Frank–Read source considered in [161] is only a few nanometers (rendering it very unlikely to exist and operate inside the grain of a real material), the above simulations suggest that it may be operational at the GBs and in reality may contribute to the dislocation slip in nanocrystalline fcc metals. It is also worth noting that the columnar simulations have shown that this anomalous dislocation multiplication can be assisted by dislocations that happen to pass by [98].

5.2. Crossover in the mechanical behavior

Both simulation studies of the mechanical behavior in the crossover regime [29,156] revealed that the transition from a dislocation-based to a GB-mediated deformation mechanisms with decreasing grain size leads to a crossover in the mechanical behavior, from Hall–Petch hardening to softening. Here, we analyze this crossover in some detail.

Fig. 21(a)–(d) provides clear evidence for a change in the deformation mechanism as the grain size decreases from 32 nm in (a), via 18 nm and 10 nm in (b) and (c), to 7 nm in (d) [29]. (The full deformation simulation for the $d = 32$ nm system is shown in *Video 4* in the supplementary material.) As in the columnar model, when the grain size becomes comparable to, or even smaller than, the size of these extended dislocations, nucleation of complete dislocations is no longer possible. Instead, as seen in Fig. 21(d), only single partials can then be nucleated, leaving behind stacking faults generated by the glide of the partials through the grains (configurations labeled (2) in Fig. 21). Having been limited to similarly small grain sizes as that in Fig. 21(d), the earlier simulations of nanocrystalline Ni and Cu by Schiotz et al. [23,91] and Swygenhoven et al. [92–94] yielded qualitatively the same behavior as that seen in Fig. 21(d). Interestingly, such incomplete nucleation events can occur even for larger grain sizes, as seen for example in Fig. 21(a). In this particular case the emission of the trailing partial appears to have been prevented by the local GB and triple-junction environments and the associated local stress fields [29]. The key question now is how this change in the deformation mechanism affects the mechanical behavior. Instead of focusing on the yield stress as a function of the grain size, Yamakov et al. [29] probed the mechanical behavior in the flow regime, by determining how the strain rate under the applied tensile stress is affected by this change in mechanism.

The plastic strain vs. time plots, $\varepsilon(t)$, shown in Fig. 23 for three of the five grain sizes studied, reveal a pronounced change in the strain rate, $\dot{\varepsilon}$, as the dislocation-slip process is gradually preempted by a GB-mediated deformation mechanism. The lack of smoothness of these curves arises from the discreteness of the deformation process, involving two distinct deformation mechanisms (see below), which is particularly noticeable due to the small number of grains in the simulation cell. It is nevertheless clear from Fig. 23 that (i) as the grain size decreases from $d = 24$ nm to 18 nm, the average strain rate decreases, and (ii) increases again as the grain size decreases further to $d = 7$ nm. Remarkably, although the deformation mechanism for $d = 7$ nm involves only GB processes (see Fig. 21(d)), the average strain rate obtained for this system exceeds even that obtained for the $d = 24$ nm system (see Fig. 23).

The deformation behavior of the system with the intermediate grain size of 18 nm is particularly revealing. The discontinuities in the slope of $\varepsilon(t)$ for this system can be correlated directly with the underlying dislocation activity (illustrated in the two insets (a) and (b) in Fig. 23, representing enlarged snapshots of the grain in the upper left corner in Fig. 21(b) taken, respectively, at $t = 70$ and 110 ps). Most importantly, the sudden, approximately five-fold increase in the strain rate occur-

ring at about $t = 105$ ps (from ~ 0.4 to $\sim 2.0 \times 10^8 \text{ s}^{-1}$) is caused by the glide of a dislocation across the grain interior (see also Fig. 21(b), taken at the same instant as inset (b) in Fig. 23). As soon as the dislocation has been annihilated in the surrounding GBs (at $t \approx 115$ ps), the strain rate decreases again. The same process is responsible for the ‘deformation bursts’ occurring at the onset of plastic deformation and at $t \approx 25$ –30 ps.

In the time intervals between these deformation bursts, no mobile dislocations exist in the structure (see inset (a) in Fig. 23). The strain vs. time behavior, for example, between $t = 30$ ps and $t = 105$ ps is therefore completely determined by GB processes. This re-

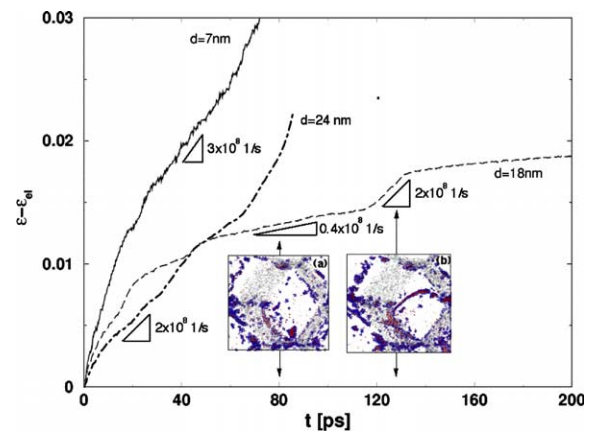


Fig. 23. Plastic strain vs. time for four-grain, fully 3d Al microstructures with grain sizes of $d = 7$, 18 and 24 nm (see also Fig. 21(b) and (d)). The strain rates indicated in several regions are given in units of 10^8 s^{-1} . The two insets (a) and (b) represent enlarged snapshots of the grain in the upper left corner in Fig. 9(c) taken at (a) $t = 70$ ps and (b) $t = 110$ ps. The colors are the same as in Fig. 21 [29] (For interpretation of the references to color in this figure legend, the reader is referred to the Web version of this article).

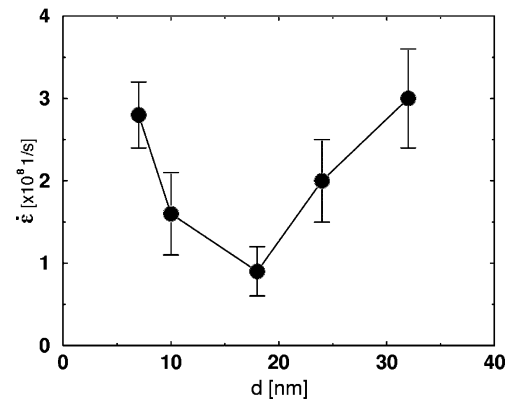


Fig. 24. Grain-size dependence of the overall strain rate for all the grain sizes studied (see also Fig. 23). The minimum in the strain rate at $d = 18$ nm suggests the existence of a ‘strongest size’ at which the grains have become too small to sustain the dislocation-slip process, but are still too large for GB processes to dominate the deformation [29].

sults in a much lower strain rate of $\sim 0.4 \times 10^8 \text{ s}^{-1}$, compared to a rate of $\sim 2.0 \times 10^8 \text{ s}^{-1}$ during the deformation bursts. The much lower deformation rate associated with the GB processes indicates that the grain size of 18 nm is still too large to enable these GB processes to fully overcome the rapidly decreasing dislocation contribution to the strain rate with decreasing grain size. On the other hand, since the dislocation-slip process is no longer fully operational for the much smaller grain size of $d = 7 \text{ nm}$ (see Fig. 21(d)), the strain rate obtained for this system must be dominated by these GB processes (see Fig. 23).

The crossover in the mechanical behavior with decreasing grain size extracted from these simulations is summarized in Fig. 24 [29]. Although for the reasons discussed above, the $\varepsilon(t)$ curves exhibit large variations, Fig. 24 shows the *average* strain rates extracted from plots like those in Fig. 23 for all five grain sizes. The minimum near $d = 18 \text{ nm}$ is clearly seen. This “strongest size” [16] of $d_c \approx 18 \text{ nm}$ for this simple Al model system is reached when the grains have become too small to nucleate complete dislocations, but are still too large for GB processes to dominate the deformation.

In qualitative agreement with all previous simulations, in the inverse Hall–Petch regime (see Section 4), the strain rate for $d = 7 \text{ nm}$ (ranging between $\sim 3.0 \times 10^8$ and $\sim 4.4 \times 10^8 \text{ s}^{-1}$; see Fig. 23) is considerably higher than that associated with the GB processes in the $d = 18 \text{ nm}$ system (of $\sim 0.4 \times 10^8 \text{ s}^{-1}$). A quantitative analysis of these results yields a ratio of the strain rate for $d = 7 \text{ nm}$ to that from 30 to 105 ps for the $d = 18 \text{ nm}$ system of between 2.1 and 2.6. Remarkably, this range of values is consistent with the mechanism of GB diffusion creep, for which Yamaoka et al. [131] showed that $\dot{\varepsilon} \sim d^{-n}$, with $2 < n \leq 3$ (see Section 4.2). This analysis suggests that in Al, even at $T/T_m \approx 0.32$, the Coble-creep mechanism is, indeed, responsible for the observed grain-size softening in the inverse Hall–Petch regime.

The recent, very large simulations of Schiotz and Jacobsen [156] for nanocrystalline Cu avoided some of the geometrical limitations of the simulation model used by Yamaoka et al. discussed above. In particular, their model system incorporated a larger number of grains and a distribution in the grain size, the average size ranging between 5 and 50 nm. The crossover in the flow stress of nanocrystalline copper thus obtained is shown in Fig. 25 [156]. Interestingly, although the stacking-fault energy of Cu is only about one third of that of Al, a comparison of Figs. 24 and 25 reveals rather similar grain sizes where the crossover from Hall–Petch to inverse Hall–Petch behavior occurs in the two materials ($d_c \sim 14 \text{ nm}$ for Cu and $d_c \sim 18 \text{ nm}$ for Al). As in the study of Yamaoka et al., this crossover in the mechanical behavior was found to be correlated with a transition in the dominating deformation mechanism.

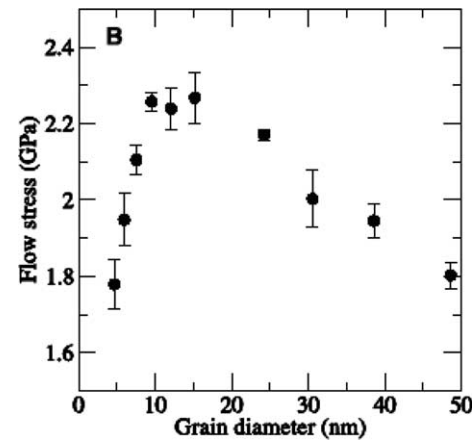


Fig. 25. Flow stress against grain size for Cu [156]. In the MD simulations the flow stress was defined as the average stress in the strain interval from 7% to 10% deformation.

While for the smallest grain sizes, Schiotz and Jacobsen [156] identified GB sliding as the dominant deformation mode, they also found that with increasing grain size the dislocation activity increases significantly. Also, as in the study of Yamaoka et al., starting at 2.5–3% plastic strain dislocations were seen to nucleate from the GBs; these were mostly partial dislocations, although in some of the larger grains several perfect extended dislocations, split into partials, were also observed. Noting that Cu has a lower SFE than Al (which decreases the energy penalty associated with the formation of a stacking fault and thus favors partial-dislocation slip over perfect-dislocation slip at grain sizes below $\sim 50 \text{ nm}$), these observations are consistent with the earlier Al simulations [29]. Remarkably, in one particularly large simulation Schiotz and Jacobsen were able to reach a 10% plastic strain for a grain size of 50 nm. These simulations revealed deformation twins in a grain-size, plastic-strain and strain-rate regime that is very close to that probed in the columnar Al microstructures [26], in which extensive deformation twinning was also observed (see Section 3.3). However, whereas the columnar simulations for a grain size of 100 nm suggested pile-ups against twin networks as the cause for the Hall–Petch hardening effect [98], for their largest grain sizes Schiotz and Jacobsen observed dislocation pile-ups against the GBs, suggesting that even in a nanocrystalline material such pile-ups can be responsible for the observed hardening.

5.3. Effect of the stacking-fault energy

Although the above comparison between Al (Fig. 24) and Cu (Fig. 25) seems to imply that the crossover grain size, d_c , may not depend very strongly on the material, the discussion in Section 3.2 has suggested that the value of d_c should be governed by the competition between the two length scales defined by the dislocation splitting

nucleation rate and, hence, the stress, σ ; $v(\sigma)$ is the velocity of the dislocation, which is also a function of σ . According to Eq. (6), equal strain rates will be reached at a given stress when the product $\rho(\sigma)v(\sigma)$ is the same in the two systems.

Up to about 0.4% plastic strain, both systems nucleate only partial dislocations propagating with about equal velocity into the grain interiors, giving rise to rather similar strain rates. At this point the two curves in Fig. 27 start to diverge. The Al(high-SFE) system is able to emit second partials which terminate these stacking faults to form complete, perfect dislocations (see Fig. 26(a)). As a result of many dislocation nucleation/absorption events, the GBs become more and more rough (see also [26]); this roughness increases the nucleation rate and leads to a continuously increasing strain rate (see the “perfect dislocation slip” regime in Fig. 27). At the same time, in the low-SFE system the second partials do not appear because, for equal stacking-fault lengths, the system energy has increased less than in the high-SFE material. Instead, the stacking faults continue to extend via the glide of the single partial dislocations. Quickly some of these transect the entire grain interior and, inevitably, block the propagation of any later formed stacking faults (see Fig. 26(b)). The inability of the low-SFE metal to produce perfect dislocations consequently leads to strain hardening, as evidenced by a continuously decreasing strain rate (see the “partial slip” regime in Fig. 27).

This situation, in which $d < r$, is similar to that in a high-SFE metal with a very small grain size (compare Fig. 26(b) with Fig. 21(d)). However, an important difference between the two materials arises from the strong d^{-3} grain-size dependence of the competing GB-based deformation process [109]. Whereas in the high-SFE metal the small grain size enables the GB-mediated deformation process to dominate, the larger grain size in the low-SFE metal favors the partial dislocation-slip process. Thus in low-SFE metals the transition from dislocation-based to GB-based deformation with decreasing grain size is more complex as these materials first undergo a transition from perfect to partial slip. As was noted by Yip [164], the existence of the partial-slip region would push the normal Hall–Petch hardening further down towards smaller grain sizes, as the partial slip produces strain-hardening, as seen in the MD simulations [114]. This reasoning suggests that lowering the SFE would result in a decrease of d_c . Indeed, a comparison of the MD simulations for Al [29] (yielding a value of $d_c = 18$ nm) with those for Cu [23] (with a SFE that is lower than that for Al, yielding a value of $d_c = 14$ nm) and with bubble-raft experiments (presumably with a very low or zero SFE, yielding a value of $d_c = 7$ nm) [165] seems to support this view [164].

These observations can be captured in a novel deformation-mechanism map based on the knowledge of dis-

location nucleation and dislocation structure in nanocrystalline fcc metals [114]. The underlying physics for this map arises from the length-scale competition between the grain size, d , and the splitting distance, r (see Eq. (1)), and from the grain-size dependence of the dislocation nucleation stress from a source at the GB proposed by Cheng et al. [107] (see Eq. (5)). In this way the map connects the mechanical properties of nanocrystalline fcc metals with the structure and physics of the dislocations present in the deformation process. Based on Eq. (1) the map is expressed in coordinates of reduced stress, σ/σ_∞ , and reduced inverse grain size, r_0/d . In contrast to the use of b and G which normalize the variables d and σ in the phenomenological constitutive equations on which the prevalent deformation maps are built [36,166–169], r_0 (the equilibrium splitting distance at zero stress) and σ_∞ (the stress at which the splitting distance becomes infinite) are material-defining parameters in this novel map. (For more details, see [114].)

According to this map the “strongest size”, d_c , may arise from two different scenarios for high- and low-SFE metals or at low and high stress. For high-SFE metals Region II [114] involves very high stress and the crossover from normal to inverse Hall–Petch behavior should be governed mainly by the transition from perfect slip to GB-mediated deformation, i.e., the $1/d$ – line between Region I and III [114]. By contrast, for low-SFE metals or under high-stress conditions, the transition involves partial slip in Region II as an intermediate stage; however, the influence of the partial slip on d_c is still not very clear. For example, Yip [164] suggested that the resulting strain hardening during partial slip may push the normal Hall–Petch behavior down to smaller grain sizes. Another consideration may be that because of the intra-grain hardening, the GB processes may become dominant at larger grain sizes in the partial-slip than in the perfect-slip regime.

5.4. Comparison with experiments

The crossover in both the dominating deformation process and the mechanical behavior shown in Figs. 24 and 25 should be reflected in the experimentally observed grain-size dependence of the yield stress (normal or inverse Hall–Petch behavior) as well as in the defect structure and texture of the plastically deformed material. In the following, we briefly review the experimental results in the light of these MD observations.

5.4.1. Normal and inverse Hall–Petch behavior

Koch and Narayan [40] recently offered a critical discussion of hardness measurements that cover the entire range of grain sizes where the crossover from ‘normal’ to ‘inverse’ Hall–Petch behavior occurs. They pointed out that the available hardness and yield-stress data may be grouped into three distinct regimes:

- (i) a coarse-grained regime, ranging from the single crystal to a grain size of about 1 μm ; in this regime the classical Hall–Petch description applies;
- (ii) a submicron grain-size regime, including grain sizes down to about 30 nm; in this regime the Hall–Petch slope is smaller than its value in coarse-grained materials, in some cases even near-zero;
- (iii) a nanometer grain-size regime, i.e., below a critical grain size below which the Hall–Petch slope is negative, hence with a decrease in strength on decreasing grain size. This behavior is often referred to as the “inverse” Hall–Petch effect.

In spite of serious experimental problems further described below, Koch and Narayan identified three observations of inverse Hall–Petch behavior that seem to be free of artifacts. Since their review, three more cases have been reported. All six ‘artifact-free’ examples reported to date are collected in Table 1.

Figs. 28 and 29 show the grain-size dependence of the hardness of nanocrystalline Ni [173] and Zn [176], respectively, prepared by laser ablation or mechanical attrition. Both measurements show the maximum in

Table 1
Nanocrystalline metals in which a crossover in Hall–Petch behavior has been reported

Material	Preparation method	References
Cu	Laser ablation	[170]
Ni	Electrodeposition	[171]
Ni	Electrodeposition	[172]
Ni	Electrodeposition	[173]
Zn	Laser ablation	[174]
Zn	Laser ablation	[175]

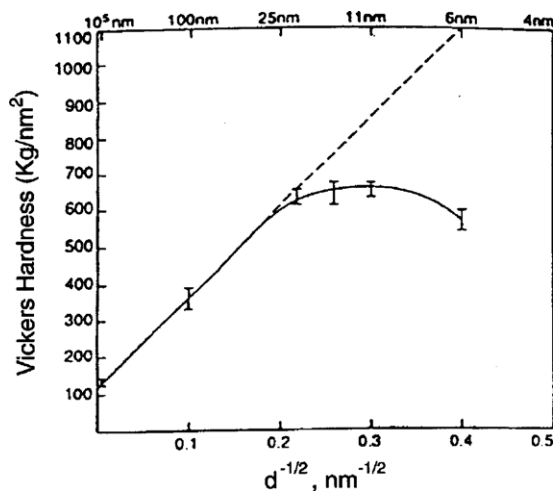


Fig. 28. Hardness of electrodeposited Ni plotted against $d^{-1/2}$ [173].

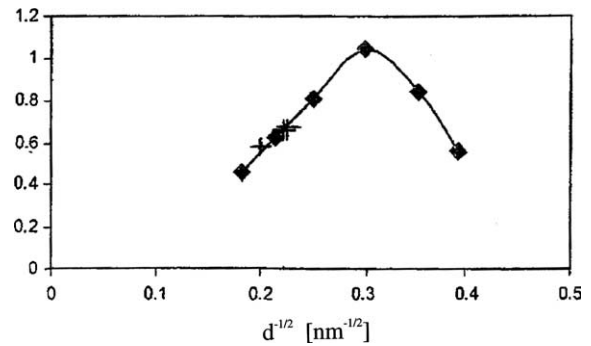


Fig. 29. Hardness of nanocrystalline Zn produced by laser ablation or mechanical attrition plotted against $d^{-1/2}$ [174].

the hardness also seen in the MD simulations as well as the transition from the normal to inverse Hall–Petch regime.

The experimental difficulties in the measurement of the mechanical properties of nanocrystalline materials result in part from the various preparation procedures applied. Materials prepared by powder consolidation (e.g., produced by inert-gas condensation or mechanical attrition) may contain pores and/or incomplete particulate bonding due to incomplete compaction [40]. This porosity may lead to an apparent “softening” at the finest grain sizes. Moreover, mechanical testing of compacted Ni powders with a grain size of 10 nm revealed [162] that both the measured strength and the tensile ductility were highly sensitive to the surface state of the samples [162]. In fact, the strength could be altered by about 50% by either coarse- or fine-polishing the sample surface. These observations agree with the results of several other studies that have demonstrated the importance of flaws in consolidated materials [150,162,177,178].

One-step production synthesis processes, such as selective pulsed-laser deposition, controlled crystallization of amorphous phases, and electrodeposition also have the potential for artifacts, however [40]. For example, crystallization of amorphous precursors can leave a residual, difficult to detect amorphous phase at the GBs, which can lead to softening and apparent inverse Hall–Petch behavior [12]. During electrodeposition, interstitial impurities and/or fine pores may be retained. For example, several groups [171,172,174,179–182] have reported yield stresses as a function of the grain size measured on nanocrystalline Ni samples prepared by electrodeposition using nominally identical deposition. While some of these measurements revealed inverse Hall–Petch behavior, others showed the conventional Hall–Petch effect. Similarly, the thermal history of the specimens (after preparation) was demonstrated to affect whether Hall–Petch or inverse Hall–Petch behavior is obtained. This was illustrated, for example, in Cu prepared by inert-gas condensation followed by consolida-

tion and annealing [13,171]. In particular, consistent with inverse Hall–Petch behavior, grain growth during annealing was found to harden the material. A similar behavior was reported by Mishra et al. [183] and Valiev et al. [184] in fine-grained Al–1.5%Mg alloys prepared by severe plastic deformation. These authors suggested that the hardening observed on annealing is due to the initial, highly non-equilibrated structure of the GBs, which may not be strong barriers to dislocation motion. However, on annealing these GBs appear to approach an equilibrium atomic structure and become dislocation obstacles.

Significant differences in GB atomic structure between that in the as-prepared state (via powder consolidation) and that in the equilibrated state (i.e., after prolonged annealing) have also been reported from X-ray diffraction studies [184] and measurements of the enthalpy stored in the GBs [80]. During annealing in vacuum, the stored enthalpy was found to decrease by about 50% without any grain growth.

Accurate determination of the grain size and its distribution represent another significant experimental problem in the analysis of hardness and strength data on nanocrystalline materials. Comparisons of the grain-size distributions obtained by TEM and X-ray diffraction studies suggest that the distributions can differ substantially [40,185]. While for the smaller mean grain sizes and for rather narrow distributions, the results obtained by the two methods matched closely, significant discrepancies existed for samples with somewhat larger grain sizes and broader distributions.

5.4.2. Microstructural observations

In Section 3.4, we already discussed some of the experimental studies on the variation of the defect structure in the deformed material in the light of the MD observations of dislocation processes, including the prediction of deformation twinning. In addition to these studies, recent measurements on the development of the deformation textures in micro- and nanocrystalline Pd [109] seem to support the MD results in Figs. 24 and 25, suggesting a transition from a dislocation-mediated to a diffusion-accommodated deformation mode.

If the plastic deformation of fcc crystals occurs by dislocation slip, characteristic textures of the deformed structure are known to develop. On the other hand, diffusion-mediated deformation processes will not result in the development of any texture because lattice diffusion in fcc metals is isotropic and deformation by GB sliding and/or GB diffusion is random relative to the crystallographic orientation of the individual crystals. The specimens used for these texture-development studies [109] were microcrystalline Pd (grain size >100 nm) and nanocrystalline Pd (11 nm grain size). Both types of specimens were initially texture free and then deformed by rolling. As seen from the pole figures in Fig. 30, the

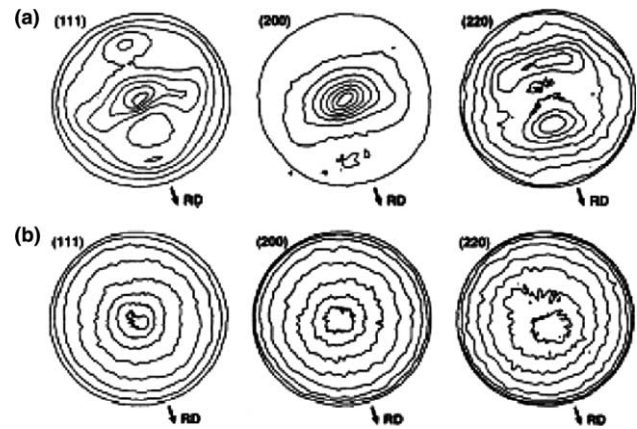


Fig. 30. Pole figures in (111), (200), and (220) direction for (a) coarse-grained Pd at a true strain of $\epsilon = 0.69$ and (b) nanocrystalline Pd at $\epsilon = 0.65$. RD indicates the rolling direction [109].

microcrystalline specimen developed the rolling texture typical for plastic deformation of fcc metals by dislocation slip during rolling. In fact, in this specimen the (111)/(200) Bragg-reflection intensity ratio, R , decreased roughly linearly as a function of the plastic strain (see Figs. 30(a) and 31); by contrast, R remained constant for the nanocrystalline specimen, suggesting that the nanocrystalline Pd did not develop any significant texture during the deformation process (see Figs. 30(b) and 31). The lack of any texture in the strongly deformed nanocrystalline Pd specimen is consistent with the features predicted by the MD simulations in the inverse Hall–Petch regime ($d < d_c$). This conclusion is further supported by the observation that the grain shape remained equiaxed at all deformations [109]. This study reported equiaxed grains in specimens deforming predominantly by GB sliding and diffusional processes; by

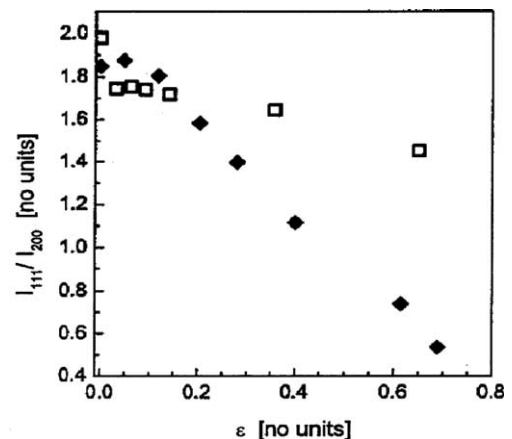


Fig. 31. Ratio of the integrated intensities I of the (111) and (200) Bragg reflection of nanocrystalline (□) and coarse grained (◆) Pd vs. ϵ [109].

contrast, dislocation slip during rolling would have resulted in elongated grains.

5.5. Critical issues and outstanding questions

Concerning the onset of plastic deformation and the question of normal vs. inverse Hall–Petch behavior, further experimental studies on well-characterized model systems are needed that avoid the specimen-preparation problems described in Section 5.4. Unfortunately no systematic studies have yet been performed to elucidate the influence of the stacking-fault energy on the yield stress as a function of grain size in either the Hall–Petch or the inverse Hall–Petch grain-size regime. Experimental studies of the relationship between the stacking-fault energy and the yield stress would provide a critical test for the predictions of the MD simulations in the crossover regime ($d \sim d_c$); in-situ measurements of internal stresses and the stacking-fault density by means of X-ray line profiling appear particularly desirable. If the transitions seen in the MD simulations, from perfect-dislocation to partial-dislocation slip and finally to diffusional processes, indeed, occur, they should be evident in the X-ray line profiles. The work of Wang et al. [118] seems to demonstrate the usefulness and feasibility of this approach.

An interesting area, not yet covered by the computer simulations of nanocrystalline materials, seems to be the generation of surface instabilities that lead to necking and failure. In all cases studied so far experimentally, the deformation of nanocrystalline materials was found to follow traditional constitutive laws for plasticity [36], differing only in the level of stress, the strain hardening and the temperature dependence. Nonetheless, pure nanocrystalline Cu was recently reported [126,127] to behave differently from coarse-grained copper concerning necking and failure. The nanocrystalline Cu displayed near-perfect elasto-plastic behavior characterized by Newtonian flow and the absence of neck formation. This observation is in contradiction to the considered criterion, which predicts instability for $d_\sigma/d_\epsilon \leq \sigma$, at constant strain rate, $\dot{\epsilon}$. Necking should have occurred soon after the yield point, as the gradient d_σ/d_ϵ tends toward zero in a near-perfect elasto-plastic regime.

Near-perfect elasto-plastic behavior has been previously reported for various metals with nanocrystalline grain sizes. Bcc iron exhibits such behavior in compression but with formation of localized shear bands, which means that these materials are prone to plastic instability [186]. Similarly, ultrafine-grained hcp titanium prepared in the same way undergoes necking in traction [173]. Elsewhere, it has been demonstrated that electro-deposited fcc nickel is able to deform superplastically at elevated temperature, two features being the absence of neck formation but high strain hardening [4]. The new

and unexpected result is that near-perfect elasto-plasticity with no work hardening can be obtained in the absence of necking. It seems that mechanical instability and its various criteria need to be examined further, both experimentally and by computer simulations.

6. Discussion and conclusions

Only a decade ago, deformation simulations of the kind reviewed above were virtually unthinkable. These simulations have now advanced far enough where they have begun not only to elucidate the structural differences between nanocrystalline and coarse-grained materials (Section 2) but also to capture the grain-size dependent mechanical behavior of nanocrystalline fcc metals (Sections 3–5). These simulations suggest the following four-stage scenario for the room-temperature mechanical behavior.

- (a) For the largest (submicron) grain sizes (see Sections 3 and 5), the GBs act as dislocation sources for the nucleation of complete, extended dislocations that subsequently glide across the grains where they become re-incorporated into the GB structure. Other than for the inability of Frank–Read sources to operate within such small grains, the material therefore still seems to deform by the conventional dislocation-slip mechanism, including for example dislocation–dislocation reactions (such as Lomer–Cottrell lock formation) and cross slip, two processes well-known from the study of coarse-grained materials and single-crystal plasticity.
- (b) As the grain size decreases well below 100 nm, the deformation behavior seems to change fundamentally, as evidenced by the observation of deformation twinning in a high-stacking-fault-energy material like Al (see Section 3.3). Remarkably, this critical prediction from the MD simulations has recently been validated experimentally, including observation of all three twinning mechanisms identified in the simulations [117,122]. Whether or not in this regime the yield-stress increase with decreasing grain size, indeed, follows the $\sigma \sim d^{-1/2}$ Hall–Petch relation has not yet been determined by simulation. However, the simulations have begun to capture two possible hardening mechanisms, including dislocation pile-ups against the GBs [156] and pile-ups against complex networks formed by deformation twins, dislocations and extended stacking faults [98].
- (c) As the grain size becomes even smaller and comparable to the size of the extended dislocations (which depends not only on the stacking-fault energy but also the applied stress; see Eq. (1)), complete-dislocation slip seems to be gradually replaced by par-

tial-dislocation slip (see Section 3.2). This important prediction from simulations of nanocrystalline Al has also been verified in recent experiments [122]. These investigators observed a deformation mechanism involving partial dislocation emission from GBs in nanocrystalline Al produced by ball milling in liquid nitrogen. The observed stacking faults (SF) were formed by the GB emission of leading and trailing Shockley partial dislocations, which is consistent with the MD simulation. There is, however, a note of caution in comparing directly this result with prediction from MD simulation. During cryomilling, there could be contamination from C, N, H, and O. As noted by the authors, these impurities may have diffused to a milled powder sample, lowering the SF energy, which led to the observation of a wider stacking fault than that predicted by MD simulation and dislocation theory.

- (d) The transition from complete- to partial-dislocation slip is accompanied by a rapid increase with decreasing grain size in the stress required to nucleate dislocations from the GBs (see Eq. (5)). The overall dislocation activity as well as their effectiveness in producing strain therefore decreases rapidly until, eventually, a GB-based deformation process takes over. The simulations reveal that this crossover in the dominating deformation mechanism gives rise to a maximum in the yield stress at the ‘strongest grain size’ d_c (see Section 5.2). Although the simulations appear to disagree as to the exact nature of the dominating deformation mechanism for $d < d_c$ (i.e., GB sliding vs. GB diffusion), it seems that the two mechanisms can be reconciled as originating from one and the same deformation process, namely Coble creep (i.e., GB-diffusion induced grain elongation accommodated by Lifshitz sliding; see Section 4.3).

Particularly at this early stage in these simulations, it is important to be aware of the fundamental limitations inherent in the MD approach (see also Section 1). In addition to being limited to relatively small, periodically repeated model systems, by their very nature MD simulations are restricted to extremely high strain rates; achieving such high strain rates, in turn, requires rather high stresses. The extreme conditions under which these simulations are usually performed therefore warrant scrutiny of any simulation results, not only by the practitioners of these simulations but also the experimental community. At a minimum the inevitably very high applied stresses must be verified to lie safely below the theoretical strength of the material for the particular mode of deformation. We add, however, that high stresses are not entirely unusual in experimental studies of nanocrystalline materials (see, e.g., [36]).

It is also critical that any new simulation result first be viewed in the context of known behavior. For example, the ability to *quantitatively* reproduce the Coble-creep formula in simulations of highly idealized nanocrystalline microstructures (see Section 4.2) offers a striking demonstration of the fact that, in spite of the high strain rates, MD simulations are capable of capturing well-known physical process which usually occur, however, on much longer time scales, thus lending credence to the unexpected deviations from the Coble-creep formula observed for the smallest grain sizes. Also, the observations of familiar dislocation reactions, such as Lomer–Cottrell lock formation and cross-slip events (see Section 3.1), lend credence to the unanticipated observations of twinning, dislocation-twin reactions and the formation of pile-ups observed at the larger strains (see Section 3.3).

As outlined above, in spite of these limitations of the MD approach, a number of important differences in the deformation behavior between coarse-grained and nanocrystalline metals predicted by MD simulation seem to be born out by experimental observations. Furthermore, one of the early findings of the MD simulation, i.e., that the atomic structures of the highly constrained GBs in nanocrystalline materials do not really differ fundamentally from those of entirely unconstrained high-energy bicrystalline GBs, is also supported by experimental observations. Also consistent with the MD simulations, a significant number of nanocrystalline materials reveal adequate plasticity in slow creep experiments where diffusional processes, including GB sliding [187], dominate. However, in several instances some experiments have reported very little ductility while other experiments on the same material, such as Cu, reported a very high ductility; see Section 4.5. Such discrepancies perhaps point not so much to any deficiencies in the simulations per se, but rather to the difficulty in assuring structural integrity in the experimental materials during the processing to produce the nanocrystalline state.

We conclude by emphasizing the promising complementarity between these types of simulations and experiments towards deconvoluting the deformation behavior of nanocrystalline materials. In spite of the well-known limitations of MD simulations discussed above, they enable the study of well-characterized, albeit idealized model systems and can thus provide insights not readily obtainable from experiments. For example, in the Coble-creep simulations the strain-rate limitation was overcome by increasing the temperature so as to speed up GB diffusion. This, in turn, required designing model microstructures with a uniform grain shape and size so as to suppress grain growth; simultaneously, this increase in temperature allowed lowering the applied stress below the threshold for the nucleation of

dislocations from the GBs. All this combined enabled identification of the intrinsic deformation behavior of this model system, unencumbered by grain growth and extrinsic effects associated with dislocations, impurities, sample porosity, etc.

In summary, we see the strength of these simulations less in their ability to one day mimic the ‘real material’ but in their ability to probe the behavior of carefully designed, fully characterized and progressively more complex model systems. This we believe will enable gradual deconvolution of the complex interplay among various deformation and microstructural processes in well-defined model systems, something that has proven difficult to achieve in experiments.

Acknowledgements

This work is supported by the US Department of Energy, BES-Materials Science under contract W-31-109-Eng-38. V.Y. is grateful for support from the DOE/BES Computational Materials Science Network (CMSN). V.Y. and S.R.P. are happy to acknowledge support by Argonne National Laboratory. A.K. Mukherjee acknowledges the support from the NSF-DMR-Metals Program. We are grateful for grants of computer time on the Cray-T3E at the John-von-Neumann-Institute for Computing in Jülich, Germany and on the Chiba City Linux cluster at ANL.

References

- [1] Gleiter H. *Acta Mater* 2000;48:1.
- [2] Koch CC, Suryanarayana C. In: Li JCM, editor. *Microstructure and properties of materials*. Singapore: World Scientific Publishing; 2000. p. 380.
- [3] Karch J, Birringer R, Gleiter H. *Nature* 1987;330:556.
- [4] McFadden SX, Mishra RS, Valiev RZ, Zhilyaev AP, Mukherjee AK. *Nature* 1999;398:684.
- [5] Kim BN, Hiraga K, Morita K, Sakka Y. *Nature* 2001;413:288.
- [6] Nieh TG, Wadsworth J. *Scripta Metall* 1991;25:955.
- [7] Siegel RW. *Mater Sci Forum* 1997;235–238:851.
- [8] Chokshi AH, Rosen A, Karch J, Gleiter H. *Scripta Metall* 1989;23:1679.
- [9] Gertsman VY, Hoffmann M, Gleiter H, Birringer R. *Acta Metall Mater* 1994;42:3539.
- [10] Erb U, Palumbo G, Zugic R, Aust KT. In: Suryanarayana C, editor. *Processing and properties of nanocrystalline materials*. Warrendale, PA: TMS; 1996. p. 96.
- [11] Masamura RA, Hazzledine PM, Pande CS. *Acta Mater* 1998;46:4527.
- [12] Alves H, Ferreira M, Koster U, Muller B. *Mater Sci Forum* 1996;225–227:769.
- [13] Fougere GE, Weertman JR, Siegel RW, Kim S. *Scripta Metall Mater* 1992;26:1879.
- [14] McMahon G, Erb U. *Microstruct Sci* 1989;17:447.
- [15] Scattergood RO, Koch CC. *Scripta Metall* 1992;27:1195.
- [16] Yip S. *Nature* 1998;391:532.
- [17] Zhu X, Birringer R, Herr U, Gleiter H. *Phys Rev B* 1987;35:9085.
- [18] Haubold T, Birringer R, Lengeler B, Gleiter H. *Phys Lett A* 1989;135:461.
- [19] Phillpot SR, Wolf D, Gleiter H. *J Appl Phys* 1995;78:847.
- [20] Phillpot SR, Wolf D, Gleiter H. *Scripta Metall Mater* 1995;33:1245.
- [21] Wang J, Wolf D, Phillpot SR, Gleiter H. *Phil Mag A* 1995;74:4786.
- [22] Allen MP, Tildesley DJ. *Computer simulation of liquids*. Oxford: Oxford Science Publications; 1987.
- [23] Schiotz J, DiTolla FD, Jacobsen K. *Nature* 1998;391:561.
- [24] Swygenhoven HV, Caro A. *Appl Phys Lett* 1997;71:1652.
- [25] Yamakov V, Wolf D, Salazar M, Phillpot SR, Gleiter H. *Acta Mater* 2001;49:2713.
- [26] Yamakov V, Wolf D, Phillpot SR, Mukherjee AK, Gleiter H. *Nature Mater* 2002;1:45.
- [27] Chen M, Ma E, Hemker KJ, Sheng H, Wang Y, Cheng X. *Science* 2003;300:1275.
- [28] Sorensen JB, Schiotz J. *Science* 2003;300:1244.
- [29] Yamakov V, Wolf D, Phillpot SR, Mukherjee AK, Gleiter H. *Phil Mag Lett* 2003;83:385.
- [30] Hasnaoui A, Swygenhoven HV, Derlet PM. *Phys Rev B* 2002;66:184112.
- [31] Hasnaoui A, Swygenhoven HV, Derlet PM. *Science* 2003;300:1550.
- [32] Daw MS, Baskes MI. *Phys Rev Lett* 1983;50:1985.
- [33] Wolf D, Merkle KL. In: Wolf D, Yip S, editors. *Materials interfaces: atomic structure and properties*. London: Chapman and Hall; 1992. p. 87.
- [34] Daw MS, Foiles SM, Baskes MI. *Mat Sci Rep* 1993;9:251.
- [35] McFadden SX, Mishra RS, Mukherjee AK. *MRS Symp Proc* 2000;601:153.
- [36] Mukherjee AK. *Mater Sci Engng* 2002;322:22.
- [37] Koblinski P, Wolf D, Gleiter H. *Interface Sci* 1998;6:205.
- [38] Coble RL. *J Appl Phys* 1963;34:1679.
- [39] Wolf D, Yamakov V, Phillpot SR, Mukherjee AK. *Z Metallkunde* 2003;1091.
- [40] Koch CC, Narayan J. *MRS Symp Proc*, vol. 634. p. B.5.1.1.
- [41] Mitra R, Ungar T, Morita T, Saunders PG, Weertman JR. In: al Y-W Ce, editor. *Advanced Materials for 21st Century*, Warrendale, PA: TMS; 1999. p. 553.
- [42] Kumar KS, Swygenhoven HV, Suresh S. *Acta Mater* 2003;51:5743.
- [43] Wolf D. In: Cahn RW, editor. *The encyclopedia of materials science and engineering*. Oxford: Pergamon Press; 2001.
- [44] Christian JW, Mahajan S. *Prog Mat Sci* 1995;39:1.
- [45] Read WT, Schockley W. *Phys Rev* 1950;78:275.
- [46] Wolf D, Jaszczak JA. In: Wolf D, Yip S, editors. *Materials interfaces: atomic structure and properties*. London: Chapman and Hall; 1992. p. 662.
- [47] Humphreys FJ, Hatherly M. *Recrystallization and annealing phenomena*. Pergamon: Oxford; 1995.
- [48] Smith CS. In: *Metals interfaces* Cleveland, OH: ASM; 1952. p. 64.
- [49] Li JCM. *J Appl Phys* 1961;32:525.
- [50] Koblinski P, Wolf D, Phillpot SR, Gleiter H. *Scripta Mater* 1999;41:631.
- [51] Koblinski P, Phillpot SR, Wolf D, Gleiter H. *Phys Rev Lett* 1996;77:2965.
- [52] Koblinski P, Phillpot SR, Wolf D, Gleiter H. *J Amer Ceram Soc* 1997;80:717.
- [53] Koblinski P, Phillpot SR, Wolf D, Gleiter H. *Acta Mater* 1997;45:987.
- [54] Koblinski P, Wolf D, Phillpot SR, Gleiter H. *Phil Mag A* 1999;79:2735.
- [55] Foiles SM, Adams JB. *Phys Rev B* 1986;40:5909.

- [56] Rosenhain W, Ewen D. *J Inst Metals* 1913;10:119.
- [57] Rosenhain W, Humfrey JCW. *J Iron Steel Inst* 1913;87:219.
- [58] Aust KT, Chalmers B. In: *Materials interfaces*. Cleveland, OH: ASM; 1952. p. 153.
- [59] Wolf D, Wang J, Phillpot SR, Gleiter H. *Phys Rev Lett* 1996;77:2965.
- [60] Pontikis V. *J de Physique (Paris)* 1988;49:C5.
- [61] Phillpot SR, Lutsko JF, Wolf D, Yip S. *Phys Rev B* 1989;40:2831.
- [62] Phillpot SR, Yip S, Wolf D. *Comp Phys* 1989;3:20.
- [63] Wolf D, Okamoto P, Yip S, Lutsko JF, Kluge M. *J Mater Res* 1990;5:286.
- [64] Wang J, Li J, Yip S, Phillpot SR, Wolf D. *Phys Rev B* 1995;52:12627.
- [65] Koblinski P, Phillpot SR, Wolf D, Gleiter H. *Phil Mag Lett* 1997;76:143.
- [66] Schoenfelder B, Wolf D, Phillpot SR, Furtkamp M. *Interface Sci* 1997;5:245.
- [67] Schoenfelder B, Koblinski P, Wolf D, Phillpot SR. In: *Intergranular and interphase boundaries in materials*. Trans. Tech. Publications; 1999. p. 9.
- [68] Mott NF. *Proc Phys Soc* 1948;60:391.
- [69] Budke E, Surholt T, Prokofjev SI, Shvindlerman L, Herzig C. *Acta Mater* 1999;47:385.
- [70] Adams JB, Foiles SM, Wolfer WG. *J Mater Res* 1989;4:102.
- [71] Yamakov V, Wolf D, Phillpot SR, Gleiter H. *Acta Mater* 2002;50:5005.
- [72] Valiev RZ, Islamgaliev RK, Alexandrov IV. *Prog Mat Sci* 2000;45:103.
- [73] Valiev R, Islamgaliev R, Yunusova N. *Mater Sci Forum* 2001;357–359:449.
- [74] Schlorke N, Weissmüller J, Dieckensheid W, Gleiter H. *Nanostruct Mater* 1995;6:593.
- [75] Fitzsimmons MR, Eastman JA, Müller-Stach M, Wallner G. *Phys Rev B* 1991;44:2452.
- [76] Löffler J, Weissmüller J. *Phys Rev B* 1995;52:7076.
- [77] Thomas GJ, Siegel RW, Eastman JA. *Scripta Metall* 1990;24:403.
- [78] Wolf D. In: Wolf D, Yip S, editors. *Materials interfaces: structure and properties*. London: Chapman and Hall; 1992. p. 1.
- [79] Raganathan S, Divakar R, Ragthunathna VS. *Scripta Mater* 2001;44:1169.
- [80] Tschöpe A, Birringer R, Gleiter H. *J Appl Phys* 1992;71:5391.
- [81] Shen TD et al. *J Mater Res* 1995;10:139.
- [82] Veprék S, Iqbal Z, Oswald HR, Webb AP. *J Phys C* 1981;14:295.
- [83] Sergueeva A, Song C, Valiev R, Mukherjee A. *J Mater Sci Engng* 2003;339:159.
- [84] Kirchheim R, Mütschler T, Kieninger W, Gleiter H, Birringer R, Koblé TD. *Mater Sci Engng* 1988;99:457.
- [85] Würschum R, Reimann K, Farber P. *Defect Diffusion Forum* 1997;143–147:1463.
- [86] Budke E, Herzig C, Prokofjev SI, Shvindlerman L. *Mater Sci Forum* 1996;207–209:465.
- [87] Konrad H, Karmonik HC, Weissmüller J, Gleiter H, Birringer R, Hempelmann R. *Physica B* 1997;234–236:173.
- [88] Ercolessi F, Adams JB. *Europhys Lett* 1994;26:583.
- [89] Noonan JR, Davis HL. *Phys Rev B* 1984;29:4349.
- [90] Hirth JP, Lothe. *Theory of dislocations*. Malabar, FL: Krieger Publishing Company; 1992.
- [91] Schiotz J, Vegge T, DiTolla FD, Jacobsen KW. *Phys Rev B* 1998;60:11971.
- [92] Swygenhoven HV, Spaczer M, Caro A. *Acta Mater* 1999;47:3117.
- [93] Swygenhoven HV, Spaczer M, Caro A, Farkas D. *Phys Rev B* 1999;60:22.
- [94] Swygenhoven HV. *Science* 2002;296:66.
- [95] Zhou SJ, Preston DL, Lomdahl PS, Beazley DM. *Science* 1998;279:1525.
- [96] Bulatov V, Abraham FF, Kubin L, Devincere B, Yip S. *Nature* 1998;391:669.
- [97] Weertman J, Weertman JR. *Elementary dislocation theory*. Oxford: Oxford University Press; 1992.
- [98] Yamakov V, Wolf D, Phillpot SR, Gleiter H. *Acta Mater* 2003;51:4135.
- [99] El-Danf E, Kalindi SR, Doherty R. *Met Mat Trans A* 1999;30:1223.
- [100] Ungar T, Ott S, Sanders PG, Borbely A, Weertman JR. *Acta Mater* 1998;46:3693.
- [101] Milligan WW, Hackney SA, Ke M, Aifantis EC. *Nanostruct Mater* 1993;2:267.
- [102] Ke M, Hackney SA, Milligan WW, Aifantis EC. *Nanostruct Mater* 1995;5:689.
- [103] Ichikawa S, Miyazawa K, Ichinose H, Ito K. *Nanostruct Mater* 1999;11:1301.
- [104] Youngdahl CJ, Weertman JR, Hugo RC, Kung HH. *Scripta Mater* 2001;44:1475.
- [105] Zupan M, Legros M, Elliott BR, Hemker KJ. In: *Advanced Materials for the 21st Century, the Julia R. Weertman Symposium*. Warrendale, PA: TMS; 1999. p. 525.
- [106] Anderson PM, Foecke T, Hazzledine PM. *MRS Bull* 1999:27.
- [107] Cheng S, Spencer JA, Milligan WW. *Acta Mater* 2003;51:4505.
- [108] Legros M, Elliott BR, Rittner MN, Hemker KJ. *Phil Mag A* 2000;80:1017.
- [109] Markmann J, Bunzel P, Liu KW, Padmanabhan KA, Birringer R, Gleiter H, et al. *Scripta Mater* 2003;49:637.
- [110] Baret CSP. *Structure of Metals*. New York: McGraw Hill; 1966. p. 196.
- [111] Klug HP, Alexander LE. *X-ray diffraction procedures for polycrystalline and amorphous materials*. New York: Wiley-Interscience; 1974.
- [112] Warren BE. *X-ray diffraction*. New York: Dover; 1990.
- [113] Ustinov A, Budarine NM. *Powder Diffraction* 2002;17:270.
- [114] Yamakov V, Wolf D, Phillpot SR, Mukherjee AK, Gleiter H. *Nature Materials* 2004;3:43.
- [115] He J, Lavernia EJ. *J Mater Res* 2001;16:2724.
- [116] He J, Chung KH, Liao X, Zhu YT, Lavernia EJ. *Met Trans A* 2002;33:1.
- [117] Liao XZ, Huang JY, Zhu YT, Zhou F, Lavernia EJ. *Phil Mag* 2003;83:3065.
- [118] Wang Y, Chen M, Zhou F, Ma E. *Nature* 2002;419:912.
- [119] Liao X, Zhao Y, Srinivasan S, Zhu Y, Valiev R, Gunderov D. *Appl Phys Lett* 2004;84:592.
- [120] Kumar K, Suresh S, Schisold M, Horton J, Wang P. *Acta Mater* 2003;51:387.
- [121] Rosner H, Markmann J, Weissmuller J. *Phil Mag Lett* 2004;84:321.
- [122] Liao XZ, Zhou F, Lavernia EJ, Srinivasan SG, Baskes MI, He DW, et al. *Appl Phys Lett* 2003;83:632.
- [123] Liao XZ, Zhao YH, Zhu YT, Valiev RZ, Gunderov DV. *J Appl Phys* 2004;96:636.
- [124] Berghazan A, Fourdeux A. *6-Eme Colloque De Saclay, 1960 Paris: Press Université; 1962.*
- [125] Li JCM. *Trans Metall Soc AIME* 1963;227:239.
- [126] Champion Y, Langlois C, Guerin-Mailly S, Langlois P, Bonnentien J-L, Hytch MJ. *Science* 2003;300.
- [127] Wang YM, Ma E. *Acta Mater* 2004;52:1699.
- [128] Swygenhoven HV, Caro A. *Phys Rev B* 1998;58:11246.
- [129] Swygenhoven HV, Derlet P. *Phys Rev B* 2001;64:224105.
- [130] Gifkins RC. *Metall Trans A* 1976;7:1225.
- [131] Yamakov V, Wolf D, Phillpot SR, Gleiter H. *Acta Mater* 2002;50:61.
- [132] Raj R, Ashby MF. *Metall Trans* 1971;2:1113.
- [133] Lifshitz IM. *Sov Phys JETP* 1963;17:909.

- [134] Langdon TG. *Mater Sci Engng* 2000;283:266.
- [135] Attwood DG, Hazzledine PM. *Metallography* 1976;9:483.
- [136] Cannon WR. *Phil Mag* 1972;25:1489.
- [137] Rachinger WA. *J Inst Metals* 1952–1953;81:33.
- [138] Ashby MF, Verall RA. *Acta Metall* 1973;21.
- [139] Weertman JR. In: Koch C, editor. *Nanostructured materials, processing, properties and applications*. Norwich, NY: Andrews Publishing; 2002.
- [140] Milligan WW. In: Karihaloo B, Ritchie RO, Milne I, editors. *Encyclopedia of Comprehensive Structural Integrity*; 2003.
- [141] Lu L, Sui ML, Lu K. *Science* 2000;287:1463.
- [142] Kim HS, Estrin Y, Bush MB. *Acta Mater* 2002;48:493.
- [143] Fedorov AA, Gutkin MY, Ovid'ko IA. *Scripta Mater* 2002;47:51.
- [144] Mara NA, Sergueeva AV, Mukherjee AK. *Mater Sci Engng* 2004;A374:244.
- [145] Hahn H, Padmanabhan KA. *Phil Mag A* 1997;76:559.
- [146] Zelin MG, Mukherjee AK. *Phil Mag A* 1993;68:1183.
- [147] Würschum R, Reimann K, Gruß S, Kübler A, Schwarwaechter P, Frank W, et al. *Phil Mag B* 1997;76:407.
- [148] Zelin MG, Dunlap M, Rosen A, Mukherjee AK. *J Appl Phys* 1993;74:4972.
- [149] Zelin MG, Mukherjee AK. *Acta Metall Mater* 1995;45:2359.
- [150] Sanders DG, Eastman JA, Weertman JR. *Acta Mater* 1997;45:4019.
- [151] Carsley JE, Fisher A, Millogan WW, Aifantis EC. *Met Mat Trans* 1998;A29:2261.
- [152] Carsley JE, Milligan WW, Zhu XH, Aifantis EC. *Scripta Mater* 1997;26:727.
- [153] Zhu XH, Carsley JE, Milligan WW, Aifantis EC. *Scripta Mater* 1997;26:21.
- [154] Hayes R, Rodriguez R, LAvernia E. *Acta Mater* 2001;49:4055.
- [155] Tabachnikova ED, Bengus VZ, Stolyarov VV, Raab GI, Valiev RZ, Csach K, et al. *Mater Sci Engng* 2001;309–310:524.
- [156] Schiotz J, Jacobsen KW. *Science* 2003;301:1357.
- [157] Ford J, Wheeler J, Movchan A. *Acta Mater* 2002;50:3941.
- [158] Moldovan D, Wolf D, Phillpot S, Mukherjee A, Gleiter H. *Phil Mag Lett* 2003;83:29.
- [159] Yamakov V, unpublished.
- [160] Bata V, Pereloma E. *Acta Mater* 2004;52:657.
- [161] de Koning M, Cai W, Bulatov V. *Phys Rev Lett* 2003;91:025503.
- [162] Dillamore IL, Smallman RE. *Phil Mag* 1965;12:191.
- [163] Orowan E. *Proc Roy Soc (London)* 1940;52:8.
- [164] Yip S. *Nature Mater* 2004;3:11.
- [165] Van Vliet KJ, Tsikata S, Suresh S. *Appl Phys Lett* 2003;83:1441.
- [166] Weertman J, Weertman JR. In: Cahn JW, editor. *Physical metallurgy*. Amsterdam: North-Holland; 1965. p. 793.
- [167] Mukherjee AK, Bird JE, Dorn JE. *Trans Am Soc Metals* 1969;62:155.
- [168] Ashby MF. *Acta Metall* 1972;80:887.
- [169] Frost HJ, Ashby MF. *Deformation-mechanism maps: the plasticity and creep of metals and ceramics*. Oxford: Pergamon Press; 1982.
- [170] Conrad H, Narayan N. *Acta Mater* 2002;50:5062.
- [171] Schuh CA, Nieh TG, Yamasaki T. *Scripta Mater* 2002;46:735.
- [172] El-Sherik AM, Erb U, Palumbo G, Aust KT. *Scripta Metall Mater* 1992;27:1185.
- [173] Sergueeva AV, Stolyarov V, Valiev RZ, Mukherjee AK. *Scripta Mater* 2001;45:747.
- [174] Narayan J, Koch CC, Zhang X, and Venkatesan R. Unpublished results, 2000.
- [175] Narayan J. *Nanopart Res* 2000;2:91.
- [176] Mukherjee AK, Mishra RS, Bieler TR. *Mater Sci Forum* 1997;233–234:217.
- [177] Fougere GE, Weertman JR, Siegel RW. *Nanostruct Mater* 1990;5:145.
- [178] Fougere GE, Riester L, Ferber M, Weertman JR, Siegel RW. *Mater Sci Engng* 1995;204:1.
- [179] Chenghe X, Mirshams RA, Whang SH, Yin WM. *Mater Sci Engng* 2001;301:35.
- [180] Hughes GD, Smith SD, Pande CS, Johnson HR, Armstrong RW. *Scripta Metall* 1986;20:93.
- [181] Thompson AW. *Acta Metall* 1975;23:1337.
- [182] Ebrahimi F, Bourne GR, Kelly MS, Mathews TE. *Nanostruct Mater* 1999;11:343.
- [183] Mishra RS, Valiev RZ, Mukherjee AK. *Mater Sci Forum* 1996;225–227:605.
- [184] Valiev RZ, Shmelik F, Bourdeaux F, Kapelski G, Baudelet B. *Scripta Metall Mater* 1992;27:885.
- [185] Nieman GW, and Weertman, J.R. In: The Morris E. Fine Symposium. The Minerals, Metals and Materials Society: Warrendale, PA, 1991.
- [186] Wei Q, Jia D, Ramesh T, Ma E. *Appl Phys Lett* 2002;81:1240.
- [187] Mukherjee AK, Mara NA, Sergueeva, AV. In: Zhu YT, editor. *Ultrafine Grained Materials Iii*. Warrendale, PA: The Minerals Metals and Materials Society; 2004.